Level 4 Milestone SP33ABM4
March 1998

Final Predictions of Ambient Conditions along the East-West Cross Drift using the 3-D UZ Site-Scale Model

Level 4 Milestone SP33ABM4

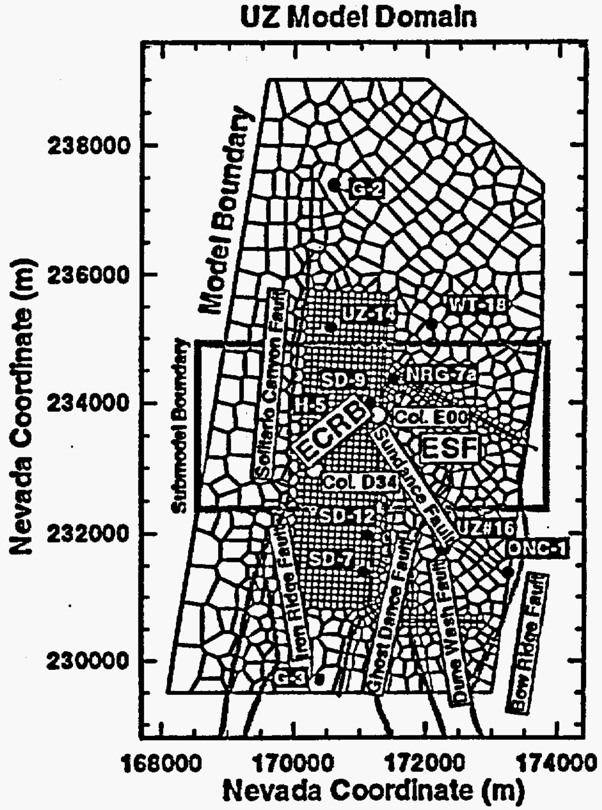

A. C. Ritcey, E. L. Sonnenthal, Y. S. Wu, C. Haukwa, and G. S. Bodvarsson

Earth Sciences Division
Lawrence Berkeley National Laboratory
One Cyclotron Road MS 90-1116
Berkeley, CA 94720

Final Predictions of Ambient Conditions along the East-West Cross Drift using the 3-D UZ Site-Scale Model

A.C. Ritcey, E.L. Sonnenthal, Y.S. Wu, C. Haukwa, and G.S. Bodvarsson
LBL Earth Sciences Division

Level 4 Milestone SP33ABM4

March 27, 1998

1.0 Introduction

In 1998, the Yucca Mountain Site Characterization Project (YMP) is expected to continue construction of an East-West Cross Drift. The 5-meter diameter drift (shown as "ECRB" on Figure 1.0-1) will extend from the North Ramp of the Exploratory Studies Facility (ESF), near Station 19+92, southwest through the repository block, and over to and through the Solitario Canyon Fault. This drift is part of a program designed to enhance characterization of Yucca Mountain and to complement existing surface-based and ESF testing studies.

The objective of this milestone is to use the three-dimensional (3-D) unsaturated zone (UZ) site-scale model to predict ambient conditions along the East-West Cross Drift. These predictions provide scientists and engineers with *a priori* information that can support design and construction of the East-West Cross Drift and associated testing program. The predictions also provide, when compared with data collected after drift construction, an opportunity to test and verify the calibration of the 3-D UZ site-scale model.

Ambient pneumatic, moisture, temperature and geochemical conditions along the drift were predicted using a series of model simulations. Flow modeling was performed using the TOUGH2 code developed by Pruess (1987; 1991). Geochemical variations were predicted using the TOUGH2 radionuclide transport module T2R3D (Wu et al., 1996). For all simulations, the 3-D UZ site-scale model grid was locally refined to explicitly discretize the proposed location of the drift, based on the basis engineering drawings and geologic cross section provided in the East-West Cross Drift Geotechnical Report (Level 3 Deliverable SP39V1M3) (TRW, 1998). A more detailed discussion of the development of the computational grid and refinement process is included in Section 3.1 of this report. Modeling was conducted using the full 3-D UZ site-scale model domain, a 3-D submodel, and a two-dimensional (2-D) cross section extracted from the full 3-D model.

This report presents data developed during a previous milestone report entitled, "Predictions of ambient conditions along the East-West Cross Drift using the 3-D UZ site-scale model" (Ritcey et al., 1998). The tracking number associated with this data is listed in Table 2.0-1.

2.0 QA Status of Work

The work performed in this study is documented in Yucca Mountain Project Scientific Notebooks YMP-LBNL-YSW-1, YMP-LBNL-GSB-1.3, and YMP-LBNL-GSB-1.9. Throughout this study, Lawrence Berkeley National Laboratory has used data collected under approved YMP Quality Assurance Procedures (QAP) whenever possible. The software packages used as part of this milestone effort include standard spreadsheet and graphics programs. Such programs are not subject to Quality Assurance (QA) requirements under the QA Requirements and Description (QARD). Hydrologic and geochemical conditions in the unsaturated zone at Yucca Mountain are characterized and simulated using the TOUGH2 code (Version 1.11) (Pruess, 1987; 1991), and the EOS3, EOS9, T2R3D, (Version 1.11) and the generalized effective continuum method (ECM) (Version 1.12) modules. This code and the associated modules have been qualified under an approved YMP QAP (Pruess et al., 1996; Wu et al., 1996). Any modifications made to this code and associated modules and used for this report, have also been qualified.

A summary of the data used in this study is presented in Table 2.0-1. This table includes a description of the data, the collecting organization, the Q status, the name of the principal investigator, and the data tracking and accession numbers (DTN and AN, respectively) used to identify the data for the YMP.

Table 2.0-1 Study Data Summary and Q Status

Borehole/Data Type Organization- Principal Investigator	Q Status	DTN/ACCN (if available)
USW SD-7/Pc, Por., S, Dp; USGS, L. Flint	Y	GS951108312231.009
USW SD-9/Pc, Por., S, Dp; USGS, L. Flint	Y	GS950308312231.004
USW SD-12/Por., S, Dp; USGS, L. Flint	Y	GS950308312231.002
USW SD-12/In-situ Pc; USGS, J. Rousseau	Y	GS960308312232.001
USW UZ-14/Pc, Por., S, Dp; USGS, L. Flint	Y	GS950308312231.005
UE-25 UZ#16/ Por., S, DP; USGS, L. Flint	Y	GS940508312231.006
Variable Infiltration Rate; USGS, A. Flint	Y	GS960908312211.003
NRG-7a/Dp, Por.; USGS, L. Flint	Y	GS951108312231.010
UZ-7a/Dp, Por, S.; USGS, L. Flint	Y	GS951108312231.011
Thermal k data; SNL, Brodsky.	Y	SNL01A07019101.001
Borehole temperature data from Sass et al. (1988)	N	GS950408318523.001/ NNA.1989.0123.0010
UZ#4, UZ#5, NRG-6, NRG-7a, SD-12, UZ-7a; /in situ gas pressure and temperature data; USGS, J. Rousseau	Y	GS960308312232.001 GS950208312232.003
Q logs for SD-9, SD-12; USGS, Moyer, Geslin and Buesch	Y	GS941208314211.060
SD-9, SD-7/ in situ gas pressure data; USGS. G. Patterson	Y	GS950808312261.003
Fracture Hydrogeologic parameters, LBNL, Wu et al., 1997	Y	LB970301233129.001
East-West Cross Drift Excavation Layout	Y	BABEAF000-01717-2100-40301-000
Air-k Permeability Data, G. LeCain, USGS	Y	GS960908312232.013
June 1997 UZ Model Milestone, Bodvarsson et al., eds., 1997	Y	LB970601233129.001
Matrix Properties of Hydrogeologic Units; USGS, L. Flint	Y	GS960908312231.004
Strontium, LANL, Triay et al., 1996	Y	LAIT.831341AQ96.001
TOUGH2 OUTPUT, Ritcey et al., 1998		LB980011233129.001
Chloride, LANL UZ Milestone	Y	NA
Por.=Porosity; S= Saturation Pc=Water Potential; Dp=Rock Grain Density		NA= Not Available; Y= qualified, N= unqualified data

The computer software used in the model calibrations and simulations in this report are Q. All data used in the report are Q, except the borehole temperature data which used both qualified (Rousseau et al., 1996) and non-qualified data (Sass et al., 1988). Nevertheless, this non-Q temperature data is consistent with the Q borehole temperature data at higher elevations, so it can be considered as corroborating evidence. In addition, a comparison of Q and non-Q data at Borehole UZ-1 by Bodvarsson et al., 1997, found that a less than 0.5 ^{o}C existed between the observed temperature profiles. Based on the assumption that the non-Q data are corroborating evidence, all model results, predictions, and conclusions presented in this report are Q.

3.0 Model Description

The simulations conducted for this analysis and the results generated are based on LBNL's conceptual model of the UZ flow system at Yucca Mountain (Bodvarsson and

Bandurraga, 1997). The 3-D UZ site-scale model grid is consistent with the Geologic Framework Model ISM2.0 (Clayton et al., 1997).

3.1 Model Domain and Grid

The 3-D UZ site-scale model domain and grid used in this study are shown in plan view in Figure 1.0-1. The model domain extends from approximately one kilometer (km) north of Borehole G-2, south roughly to Borehole G-3, and from the Bow Ridge Fault in the east to about one km west of the Solitario Canyon Fault. This grid is similar to the grid used in LBNL's FY97 Milestone Report (Haukwa and Wu, 1997); however, it was locally refined along the proposed location of the East-West Cross Drift. In other words, individual elements were added to the existing 3-D UZ site-scale model grid to represent the drift. These new elements were added at the same elevation as the proposed drift alignment. They were also oriented along the proposed drift alignment. The volume of each cylindrical element was calculated using the length of the element and assuming the diameter of each element is equivalent to the proposed 5 meter drift diameter. Each drift element was connected to adjacent drift and non-drift elements. Because this modification changed the UZ grid only in the vertical direction, it would be visible only along a cross section that sliced vertically across the 3-D UZ site-scale model grid along the drift alignment. The drift shown on the plan view figure 1.0-1 shows the proposed alignment of the grid projected to the surface.

Also shown on Figure 1.0-1 is the approximate location of a 3-D submodel domain extracted from the 3-D UZ site-scale model domain. This 3-D submodel was used for temperature, pneumatic and geochemical predictions because it is less computationally intensive and allowed more simulations to be conducted than would have been feasible if the full 3-D UZ site-scale model was used. The full model and submodel boundaries are all located sufficiently far from the proposed East-West Cross Drift so that their effects at the drift are negligible. A 2-D cross section, which corresponds to the proposed drift location, was also extracted from the 3-D UZ site-scale model. This 2-D cross section was used for dual-permeability (dual-k) geochemical predictions.

The layering and subdivision of geological units in the numerical grid are based on the geological model used in LBNL's 1997 milestone (Hinds et al., 1997). Grid layers have spatially variable thicknesses across the model. Lateral geologic variations, such as pinch-outs and zeolitic alteration, are represented. The 3-D UZ site-scale model grid has a maximum of twenty-eight grid layers that represent different hydrogeological units and alteration zones in the unsaturated zone of Yucca Mountain. The Tiva Canyon unit (TCw) is vertically subdivided into three layers, although some of these layers are not present in all locations due to erosion. The Paintbrush unit (PTn) is represented using five grid layers where these hydrogeologic layers exist. The Topopah Spring unit (TSw) is divided into seven sublayers and an additional three layers are used for the repository area. The Calico Hills unit (CHn) has a maximum of eight sublayers, but generally five layers in most locations. The 3-D UZ model grid (ECM) has 40,577 elements, and 136,200 connections between the blocks. The 3-D UZ model grid (dual-k) has 78,214 elements and over 310,000 connections. The 3-D submodel grid (ECM) has about 18,000 elements and 60,000 connections. The 2-D cross section (dual-k) has approximately 2,000 elements and 4,600 connections.

All major faults (offset greater than 20 m) from the Geologic Framework Model ISM2.0 (Clayton et al., 1997), including the Solitario Canyon, Iron Ridge, Ghost Dance, Abandoned Wash, and Dune Wash faults, are incorporated explicitly in the 3-D UZ site-scale model, and most are shown in Figure 1.0-1. Faults are represented in the model as vertical zones with sharp stratigraphic offsets and connections to adjacent grid layers. The Sundance Fault, which is a northwest-striking fault zone with a maximum cumulative displacement of 11 m (Potter et al., 1995) is also shown on Figure 1.0-1. Because this fault is expected to be intersected by the East-West Cross Drift, but is not incorporated into the model grid, some uncertainty in model predictions is expected in this area. This uncertainty could occur because local features such as offset in cooling joints, brecciation or zones of intense fracturing may exist that have not been considered by the model. Uncertainty in model predictions is also expected where the East-West Cross Drift intersects the Solitario Canyon Fault. This fault, which has offset as large as hundreds of meters (Kwicklis et al., 1996), is discretized in the model grid as a vertical zone with sharp stratigraphic offset and connections to adjacent grid layers. However, the grid in the fault zone does not consider detailed local variations in the amount of offset, surficial units exposed, and rock properties that could decrease or increase the flow of water and air within these zones. In particular, surficial outcrops of the TSw hydrogeologic unit at the fault zone may allow water and air to be introduced directly into this unit, and offsets that place the highly fractured TCw adjacent to the TSw also are expected to affect the movement and distribution of water and air in this region. Transient flow behavior may also be important in this fault zone because the PTn hydrogeologic unit is not present to act as a dampening unit. Transient flow such as this is not captured by a steady-state model.

The hydrogeologic units in the 3-D UZ site-scale model correspond to the major hydrogeologic units and alteration zones as shown in Table 3.1-1. Development of model layering is described in Bandurraga (1996) and Wu et al. (1997).

Table 3.1-1 Relationship between Model Hydrogeological Units and Geological Formations.

Geological Unit	Welding Intensity/ Formation Name (Buesch et al., 1995)	Model Unit	Hydrogeological Unit
PAINTBRUSH GROUP			
Tiva Canyon Tuff	M,D[1] (Tpcxxxx)	tcw11 tcw12	Tiva Canyon (TCw)
	D- Basal Vitrophyre (Tpcpv3) M (Tpcpv2)	tcw13	
	N,P (Tpcpv1)	ptn21	Paintbrush (PTn)
Bedded tuff	N (Tpbt4)		
Yucca Mountain Tuff	N,P,M (Tpy)	ptn22	
Bedded tuff	N (Tpbt3)	ptn23	
Pah Canyon Tuff	N,P,M (Tpp)	ptn24	
Bedded tuff	N (Tpbt2)	ptn25	
Topopah Spring Tuff	N,P (Tptrv3)		
	M (Tptrv2) D -Upper vitrophyre (Tptrv1)	tsw31	Topopah Spring (TSw)
	M,D (Tptrn)	tsw32	
	M,D,L (Tptrl) M,D,L (Tptpul)	tsw33	
	D (Tptpmn)	tsw34	
	M,D,L (Tptpll)	tsw35	
	D (Tptpln)	tsw36	
	D (Tptpv3)	tsw37	
Bedded tuff	N,P,M; may be altered (Tptpv1, Tptpv2) N; may be altered (Tpbt1)	ch1 (vc or zc)	Calico Hills (CHn)
Calico Hills Formation	N; unaltered (Ta - Vitric)	ch2vc	
	N; altered (Ta - Zeolitic)	ch3zc	
	N; may be altered (Thtbt)	ch4 (vc or zc)	
CRATER FLAT GROUP			
Prow Pass Tuff	N; may be altered (Tcp) Unit 4[3]		
	P,M Unit 3	pp3vp	
	N,P; generally altered Units 2,1	pp2zp	
Bedded tuff	N; generally altered (Tcpbt1)		
Upper Bullfrog Tuff	N,P; generally altered (Tcb)		
Middle Bullfrog Tuff	P,M	bf3vp	
Lower Bullfrog Tuff	N,P; generally altered	bf2zp	Crater Flat Undifferentiated (CFu)
Bedded tuff	N; generally altered (Tcbbt)		
Upper Tram Tuff	N,P; generally altered (Tct)		

[1] Welding Intensity N=Non-; P=Partially; M=Moderately; D=Densely

[2] L=Lithophysal Zone

[3] Units per Moyer and Geslin (1995)

3.2 Boundary Conditions

The top model boundary represents the ground surface of the mountain or, where present, the bottom of the alluvium. The bottom boundary of the model represents the potentiometric surface, which is a relatively flat, stable surface in the vicinity of the East-West Cross Drift. Both top and bottom boundaries of the model are treated as Dirichlet boundaries (constant, but distributed gas pressures and temperatures, and constant liquid saturations), except in the EOS3 module simulations that allowed surface gas pressure to vary. Gas pressure conditions at the bottom boundary of the model are calculated relative to an observed pressure value of 0.92 bars at an elevation of 730 m (Ahlers et al., 1995a&b), using an equation that calculates atmospheric pressure as a function of altitude.

The initial surface gas pressure conditions were determined by running TOUGH2 to steady-state using specified bottom gas pressure, specified top and bottom boundary temperatures, and applied surface net infiltration conditions. This is necessary to generate a steady-state, equilibrated gas pressure boundary at the surface that will avoid artificial air flow or circulation, which may happen when non-equilibrated pressures are imposed on the ground surface boundaries. All lateral boundaries (shown in Figure 1.0-1) are treated as no flow boundaries. This treatment is reasonable for the eastern boundary, since high vertical permeability and lower capillary forces are expected along the Bow Ridge Fault. For the southern, western, and northern lateral boundaries, no flow boundaries should have little effect on moisture flow movement and distributions in the vicinity of the potential repository, since these boundaries are all located at a minimum of 750 m from the conceptual repository boundary.

Bottom boundary temperatures were taken and interpolated from the borehole temperature data measured at the water table by Sass et al. (1988). These temperature data, which have an average value of about 32°C, are also consistent with data determined by Fridrich et al., (1994).

To account for differences in ground surface temperatures on the mountain at different elevations, we used both an observed borehole temperature data and the following theoretical equation that correlates temperature with elevation (Lu and Kwicklis, 1995):

$$T_s = T_{ref} + \lambda \,(Z_{ref} - Z) \qquad \text{Eqn: 3.2-1}$$

where T_s is the ground surface temperature to be determined at elevation Z; T_{ref} is the temperature at the reference elevation , Z_{ref}, and λ is the atmospheric lapse rate (°C/m), a constant to be determined. The surface temperatures are estimated using observed temperature data from Boreholes NRG-6 and NRG-7a, which include over a year of continuous temperature monitoring (Rousseau et al., 1996).

Using the surface elevation data and an annually averaged temperature of 18.23°C at NRG-6 and 17.78°C at NRG-7a (Rousseau et al., 1996), we can calculate the atmospheric lapse rate to be ≈ 0.01 °C/m at Yucca Mountain. The surface temperatures were then determined using Equation 3.2-1 and the elevations of the uppermost grid blocks of the model. The resulting surface temperature distribution has an average temperature of 19°C. Lower than average surface temperatures were calculated where elevations are higher, along the ridgetop and in the northern part of the mountain.

Thermophysical properties of liquid water and vapor are internally generated in the TOUGH2 code within experimental accuracy from steam table equations (International Formulation Committee, 1967). Air is treated as an ideal gas, and the additivity of partial pressures is assumed for air/vapor mixtures.

The spatial distribution of net infiltration along the top ground surface boundary was taken from a recent USGS net infiltration map (Flint et al., 1996). This infiltration map (Figure 3.2-1) estimates an average infiltration rate of 4.9 mm/yr distributed over the 3-D UZ site-scale model domain. Higher infiltration rates are located at the northern part of the model domain, near Borehole G-2, and along the north-south ridge of the mountain. Lower infiltration rates are located at and near the Bow Ridge Fault (the eastern boundary) and in the southwest corner of the model. Two additional infiltration scenarios were simulated by increasing the infiltration rates applied as an initial upper boundary condition by a factor of five and also decreasing these infiltration rates ten-fold. These scenarios were used to help bound uncertainty in temperature predictions. Infiltration was increased and decreased three-fold for the dual-k model to bound saturation predictions. Infiltration scenarios were different for the temperature and saturation predictions because temperature is less sensitive to changes in infiltration than saturation.

3.3 Model Parameters

The simulations conducted for this analysis and the results generated are based on LBNL's dual-k, base-case, parameter set "Qb" documented in LBNL Milestone SLX01LB1 provided for TSPA-VA (Wu et al., 1997) (see Appendix A, Tables A-1a, A-1b, A-2a and A-2b). This spatially varying property set was calibrated through an inverse modeling process that involved matching saturation and water potential profiles in individual boreholes against measured data using ITOUGH2 (Finsterle, 1993) as well as calibrated against available temperature, pneumatic, geochemical, and perched water data (Bandurraga and Bodvarsson, 1997; Bandurraga et al., 1997; Wu et al., 1997a).

As described in Section 3.2, Boundary Conditions, several scenarios were considered to bound uncertainty in infiltration estimates. For the ECM model, which was used for steady-state pneumatic and 3-D geochemical simulations, infiltration rates applied as an upper boundary condition were increased five-fold and decreased ten-fold. For the dual-k model simulations, infiltration was increased and decreased three-fold to bound saturations predicted along the drift. Properties that were added to the base-case, dual-k parameter set "Qb" (Wu et al., 1997), to calibrate the 3-D UZ site-scale model with perched water data, were removed for the 3-D submodel (ECM) and the 2-D cross-section (dual-k) simulations to increase computational efficiency. Because perched water occurrences at Yucca Mountain are located below the proposed elevations of the East-West Cross Drift, removal of these parameters should have no impact on predictions along the drift. For comparison, simulations conducted with the full 3-D UZ site-scale model domain retained these perched water properties.

The "Q" thermal properties used for the temperature predictions (Ho and Francis, 1997) are listed in the Appendix A, Table A-3. Thermal conductivity was calculated by TOUGH2 using a linear interpolation formula that determined conductivity as a function of liquid saturation.

3.4 Numerical Formulation

Modeling for this study was conducted using TOUGH2, a multiphase, integrated finite difference code developed by Pruess (1991), and the EOS3, EOS9, ECM, and T2R3D modules. A key criterion for selecting the numerical formulation appropriate for a highly fractured, heterogeneous system such as Yucca Mountain is the manner in which fracture-matrix interaction is treated. This study uses both the ECM (Wu et al., 1996) and the dual-k approaches to treat fracture and matrix flow. In the dual-k approach, fracture and matrix systems are treated separately as two parallel, overlapping, and continuous media with interactions at each location. The ECM defines characteristic curves for fracture and matrix flow independently, and reasonably approximates steady-state systems where the equilibrium condition is met (Doughty and Bodvarsson, 1996; Wu et al, 1996a; Doughty and Bodvarsson, 1997). In this report, the dual-k approach was used for saturation and percolation flux predictions and the ECM approach was used for the temperature and gas pressure predictions. Geochemical predictions were made using both the ECM and the dual-k approaches. It has been shown (Doughty and Bodvarsson, 1996; Wu et al, 1996a) that the ECM formulation accurately describes fracture/matrix flow for steady-state moisture, heat flow and gas flow for the UZ system at Yucca Mountain. The ECM is also computationally simpler to use. The dual-k approach, which is more rigorous than the ECM approach for some applications (Doughty and Bodvarsson, 1996), is more computationally intensive.

The TOUGH2 EOS9 module, which efficiently solves an approximation of Richard's equation assuming gas to be passive, was used for the saturation and percolation flux predictions. This approximation is adequate for saturation and percolation flux predictions where liquid flux is the primary component of interest (Doughty and Bodvarsson, 1996). The more rigorous TOUGH2 EOS3 module, which treats air and water as separate components, was used for temperature and gas pressure predictions.

4.0 Predictions

4.1 Saturation, Water Potential, and Percolation Flux Predictions

Methods

Saturations, water potentials and percolation fluxes were predicted along the East-West Cross Drift using the full 3-D UZ site-scale model grid. The dual-k formulation was used to treat flow between the fractures and the matrix. In addition to the base-case infiltration scenario, infiltration was increased and decreased three-fold to bound saturations predicted along the drift. Results were obtained using the TOUGH2 EOS9 module.

Predictions and Uncertainties

Figures 4.1-1 through 4.1-6 show saturations contoured along the East-West Cross Drift extracted from the 3-D UZ site-scale model. The gray scale used for fracture saturations is different from the scale used for the matrix saturations in order to improve figure visibility and reproduction quality. The results show higher saturations resulting from the higher infiltration scenarios and lower saturations resulting from the lower infiltration scenarios. Saturations are also generally lower on the east end of the drift where infiltration rates applied as a surface boundary condition are lower. Fully saturated conditions are found in the CHn hydrogeologic unit below the East-West Cross Drift. This predicted perched water zone is consistent with the current conceptual model of perched water locations in the North Ramp region. Saturations are also much lower near the Solitario Canyon Fault where hydraulic conductivities are larger than nearby zones. As discussed in Section 3.1, the spatial discretization of the 3-D UZ site-scale model grid along the Solitario Canyon Fault is not able to adequately capture the impact of local features such as variations in the amount of offset, surficial units exposed, and rock properties that would be necessary to make more accurate predictions in this area. Excluding the Solitario Canyon Fault zone, matrix saturations along the drift ranged from about 0.66 to 0.92, and fracture saturations along the drift ranged from about 0.04 to 0.12. These saturation values indicate that perched water is unlikely to be intersected during drift excavation. Increasing and decreasing infiltration changed matrix saturations by approximately 0.03 to 0.04, depending on location. Figure 4.1-7 shows simulated matrix water potentials along the drift for the base-case, infiltration multiplied by three and infiltration divided by three scenarios. Water potentials range from approximately -150 to -600 kPa for the base case, from approximately -100 to -450 kPa for the infiltration multiplied by three scenario, and from approximately -300 to -700 kPa for the infiltration divided by three scenario. In Figure 4.1-8, which again illustrates modeled saturations along the drift, "Qf", "Qfd3" and "Qfx3" represent the fracture saturations for the base-case, the infiltration divided by three, and the infiltration multiplied by three scenarios, respectively. "Qm", "Qmd3" and "Qmx3" represent the matrix saturations for these three cases. Because the 3-D UZ site-scale model is based on a layer-averaged parameter set that may not incorporate small-scale local heterogeneities, some uncertainty in saturation predictions is expected. Figure 4.1-9 shows percolation fluxes predicted along the drift for the base-case and infiltration decreased and increased three-fold scenarios. The fluxes predicted range for the base-case infiltration scenario ranged from approximately 0 to 17 mm/yr. For the infiltration multiplied three-fold scenario, percolation fluxes ranged from 0 to 50 mm/yr. For the infiltration decreased three-fold scenario, percolation fluxes ranged from 0 to 6 mm/yr. The predictions do not consider the impact of drift excavation on percolation fluxes. Some uncertainty may also be expected where the Solitario Canyon Fault intersects the drift.

4.2 Gas Pressure Predictions

Methods

Steady-state gas pressures were predicted along the East-West Cross Drift using the 3-D submodel grid. The submodel domain is shown in Figure 1.0-1. Fracture/matrix interaction was treated using the ECM. The TOUGH2 EOS3 module was used for the simulations, and gas pressure was fixed at the lower model boundary (the potentiometric surface). The base-case infiltration scenario was applied as a surface boundary condition and no additional infiltration scenarios were considered.

Predictions and Uncertainties

Figure 4.2-1 shows gas pressures predicted along the East-West Cross Drift. Steady-state gas pressures ranged from approximately 88.0 to 88.5 kPa. Field observations of gas pressures, which may be expected to vary based on daily and seasonal changes by as much as 2 kPa, can only be predicted using a transient model. The shaded areas shown on Figures 4.2-1 and 4.2-2 represent the range of this uncertainty. Excavation of the drift is also expected to impact observed gas pressures; however, these effects have not been considered in these predictions. Figure 4.2-2 shows a one-dimensional (1-D) gas pressure profile along a single column extracted from the 3-D submodel results. The location of the column is shown in Figure 1.0-1. Steady-state gas pressure increases with depth as a function of altitude.

4.3 Thermal Predictions

Methods

Steady-state temperatures were predicted along the East-West Cross Drift using the 3-D submodel grid. The submodel domain is shown in Figure 1.0-1. Fracture/matrix interaction was treated using the ECM. The TOUGH2 EOS3 module was used for the simulations, and spatially-varying top and bottom temperatures were specified. Three infiltration scenarios, the base-case infiltration scenario, infiltration increased five-fold, and infiltration decreased ten-fold, were modeled to consider the impact of uncertainty in infiltration estimates on temperatures predictions. For temperature predictions, the range in infiltration scenarios was larger to consider uncertainty in infiltration estimates and sensitivity to temperature. Before making any predictions the model was calibrated by adjusting top and bottom temperatures to match observed data at fifteen boreholes located within the submodel domain. Four boreholes where Q data were available (Boreholes UZ#4, UZ#5, NRG-6 and NRG-7a) (Rousseau et al., 1996) and eleven boreholes where non-Q data were available (H-6, a#1, B#1, A#6, a#6, H-5, a#4, a#5, WT#4, H-1, and G-1) (Sass et al., 1988) were used for the calibration. Figure 4.3-1, which shows a comparison between an observed and modeled temperature profile at Borehole H-5, demonstrates the results of the calibration process.

Predictions and Uncertainties

Figures 4.3-2 shows temperature contoured along an east-west cross section extracted from the 3-D submodel. The location of the East-West Cross Drift sketched on the figure is approximate. Temperatures ranged from about 22 to 25 degrees Celsius, with lower temperatures below the ridge top and near Solitario Canyon along the western portion of the cross section. Figure 4.3-3 shows the predicted temperatures along the East-West Cross Drift along the drift location. The shaded area on the figure represents the range of predicted temperatures at a given point. This range reflects uncertainty in temperature predictions due to variability in top and bottom temperatures, and equals the value of the modeled temperature at each location plus or minus two standard deviations based on the range in calibrated bottom boundary temperatures. Uncertainty in temperature predictions also exists due to uncertainty in infiltration estimates, but is not shown on the figure. Figures 4.3-4 and 4.3-5 show two 1-D temperature profiles extracted from 3-D submodel results. The location of the columns are shown in Figure 1.0-1. The ranges of predicted temperatures are also shown on these figures. This range is also based on the range in calibrated bottom temperatures, and does not consider uncertainty in infiltration estimates. Figure 4.3-6 shows the range in temperatures predicted for the base-case, infiltration increased five-fold and infiltration decreased ten-fold scenarios. This figure shows the uncertainty in temperatures predictions due to uncertainty in net infiltration estimates and climate.

4.4 Geochemical Predictions

Methods

The prediction of chloride concentrations was performed by the method outlined in Sonnenthal and Bodvarsson (1997). The simulations were run using the T2R3D module, which solves the conservation equations for water, air, and a chemical component simultaneously (Wu et al., 1996). The diffusion coefficient for Cl in water was set to 1e-10 m^2/s[1] in the matrix and approximately 1e-10 m^2/s in fractures (the actual value at a given node varies somewhat due to local fracture-matrix connection areas). Because of the coarseness of the model, we assume dispersivity to be zero. All runs were performed under isothermal conditions (uniform 25° C in the 2-D simulations and a constant yet spatially variable temperature field determined from steady-state simulations in the 3-D model). Boundary conditions are no mass flux at the sides and base, for air, water and chemical components. Water and chemical components are set with a mass flux at the upper boundary, discussed below. Boundary conditions for flow are identical to those described previously, and all other parameters are identical to those used in the flow simulations described previously, with the steady state flow fields from the flow simulations.

The chloride flux to the surface was calculated from the precipitation maps provided by the USGS (Flint et al., 1996) and the most recent estimated mean effective Cl concentration in precipitation (0.62 mg/liter; Fabryka-Martin, 1998). The effective concentration is concentration in rain plus the contribution from soluble airborne particulates (Fabryka-Martin et al., 1996) and is assumed to be constant over time (Tyler et al., 1996). Four simulations were performed to model the Cl distribution under steady conditions for the present and glacial maximum climates and a transient simulation assuming that there was an abrupt change in climate 10,000 years ago, as follows:

1. 3-D ECM submodel of UZ Site-Scale model using modern precipitation and infiltration rates (steady-state).

2. 2-D dual k model using modern precipitation and infiltration rates (steady-state).

---

[1] The true value may be greater than this (Oldenburg and Pruess, 1995) ; however, given the coarseness of the model grid and the resultant numerical dispersion, a higher value may give an unrealistic value of the total dispersivity.

3. 2-D dual k model using glacial maximum precipitation and infiltration rates (steady-state).

The steady-state transport simulations were run for nearly 1 million years, and may differ a few percent at most from true steady state concentrations, because all simulations are run in a transient mode until the values change by less than a prescribed value, usually a small fraction of a percent. Given the small time step needed for transport, the computer needed requires a slightly relaxed criteria. The maximum differences of a few percent are very small compared to the two orders of magnitude range in concentrations. Time steps were limited to a maximum of 100 years to ensure that numerical oscillations are not present. This maximum time step is obtained from the consideration that the transport distance in a given time step should not exceed the grid block dimension.

4. 2-D dual permeability transient simulation using modern infiltration and precipitation applied to the glacial maximum precipitation and infiltration concentration and flow distributions for a period of 10,000 years. This is meant to evaluate the effect of a climate change on the chloride concentrations.

One simulation was performed to predict the strontium concentrations in the cross drift. The Sr concentrations were predicted in a manner similar to the chloride concentrations, except that it is considered to be nonconservative in zeolitic units. Because all of the strongly zeolitized rocks are below the repository, exchange with zeolites has no effect on the model predictions for Sr in the planned cross drift. The exchange coefficient for Sr in zeolites was set to $1 m^3/kg$ (Triay et al., 1996). The effective concentration in precipitation was set to .0058 mg/liter (Triay et al., 1996). One ECM 3-D simulation was performed using the modern precipitation and infiltration conditions, similar to the chloride simulations.

Background ^{36}Cl/Cl values were estimated from the chloride concentrations, assuming a climate change at 10,000 Ka and an approximate shift in the ^{36}Cl/Cl ratio from 1000e-15 to 500e-15. The assumption is that the change in the chloride concentration in the climate change simulation reflects the proportion of modern water added to the glacial maximum concentrations, as follows:

$$^{36}\text{Cl/Cl (predicted)} = X*500 + (1-X)*1000 \qquad (4\text{-}4.1)$$

where,

$$X = (C_{CC} - C_{GM})/(C_M - C_{GM}) \qquad (4\text{-}4.2)$$

and C_{CC} is the concentration from the climate change simulation, C_{GM} is the concentration at the the last glacial maximum (assumed to have persisted to 10,000 years ago), and C_M is the modern concentration (steady-state value). The fractional change in concentration between the simulations is given by X.

Predictions and Uncertainties

Chloride

Figures 4.4-1 and 4.4-2 show the modeled chloride concentrations for the modern infiltration regime. Figure 4.4-1 is a 2-D cross section from the 3-D ECM model, and Figure 4.4-2 shows the fracture chloride concentrations from the 2-D dual-permeability simulation. They are nearly identical, except at the model domain sides which do not receive fluxes from surrounding gridblocks in the 2-D model as in the 3-D model. Fracture and matrix concentrations are also nearly identical for the dual permeability steady-state simulations. Figure 4.4-3 shows the transient simulation of modern infiltration and chloride fluxes applied to the steady-state glacial maximum chloride and liquid saturation distribution, assumed as the initial conditions. Regions of high infiltration (under Yucca Ridge) are similar to the modern concentrations, because the modern fluxes are sufficient to displace and dilute the previous waters almost completely. Under regions of lower infiltration, on the west and on the east sides, the depths of modern water penetration are substantially less.

Figure 4.4-4 shows the concentrations for all of the chloride simulations plotted as a function of the Nevada State Plane East (NSP-E) coordinate at the approximate level of the planned cross drift (elevation about 1100 m). Less emphasis should be placed on the east and west boundaries of the model, which only receive fluxes from downdip elements and therefore are closer to values as obtained from a 1-D simulation. Although the lower infiltration rates in these regions should give higher concentrations, they are not likely to be as pronounced as the model predicts. The profiles show that for the steady-state modern climate simulations, the ECM and dual permeability runs (matrix chloride (shown) and fracture chloride (not shown)) give nearly identical results. This shows also that flow to the repository level is generally well-predicted by a 2-D model. Below the repository, there is considerable lateral flow, mixing effects are more important (Sonnenthal and Bodvarsson, 1997), and thus large-scale 3-D models should be employed to model concentration variations. The climate-change simulation shows an interesting break at about NSP-E 170850 m, where on the west side the matrix concentrations are almost the same as the modern concentrations, whereas on east side they are close to the glacial maximum concentrations. Fracture chloride values have equilibrated nearly everywhere with the modern chloride concentrations in fractures, yet still showing strong disequilibrium with some matrix blocks. The lack of chloride equilibration between pore waters in matrix and fracture blocks displays well the effect of slow mixing and chemical diffusion in the matrix pore waters.

Based on the interpreted level of mixing of older glacial waters with younger waters seen in the perched water bodies and in the Calico Hills units (Yang et al., 1996; Sonnenthal and Bodvarsson, 1997; Fabryka-Martin et al., 1998), it should be expected that there is still some component of pore waters from the wetter climate prevailing before 10,000 years ago in the matrix blocks. Fracture waters should show near-modern concentrations. Therefore, samples of pore waters taken from matrix blocks may show a range of concentrations, between the modern and climate change values. On the west side, the fracture and matrix chloride concentrations are nearly identical, but on the east side there is a large difference in matrix and fracture pore water concentrations and greater variations in the concentrations should be expected. This could be due to variable amounts of mixing and the sample location relative to fractures that may have transmitted differing fluxes.

Uncertainties in the predicted chloride concentrations are directly a function of the uncertainty in the infiltration and precipitation rates. The effective mean concentration in modern precipitation could differ up to a maximum of about 30% (see bounds described in Sonnenthal and Bodvarsson, 1997), resulting in concentrations 30% higher or lower. Local variations in chloride fluxes could also be different due to spatial variations in dust accumulation, although this has not been documented.

Strontium

Strontium concentrations from the 3-D ECM model are plotted in Figure 4.4-5 for the cross-section along the planned cross-drift. They show a similar pattern to the chloride concentrations, except where zeolites are encountered in the Calico Hills and the pore water concentrations drop off precipitously, due to strong exchange. The exchange coefficient was set to zero along the western margin, in the Solitario Canyon Fault, and therefore there is no reduction in concentrations evident here. Because the purpose of this model was to predict concentrations in the cross-drift, the regions below should not be considered well-constrained, because the larger-scale effects of lateral flow obtained in the full 3-D site-scale model are not present. A plot of Sr concentrations along the level of the drift is shown in Figure 4.4-6. Except for the side boundaries, which are less reliable, the concentrations are in the range of about 0.05 mg/liter to about 0.3 mg/liter. Given that the measured concentrations in Yucca Mountain pore and perched waters vary from about 0.003 mg/liter to over 1.2 mg/liter (Sonnenthal et al., 1997), the range predicted here is fairly narrow.

The effective concentration of Sr in precipitation is less constrained than that for chloride, owing to the paucity of measurements. The presence of Ca-rich zeolites in the PTn could result in much lower concentrations than that predicted here, owing to exchange. Slightly higher concentrations could occur due to water-rock interaction by dissolution of volcanic glass in the bedded tuffs, but this effect would not shift them more than about 50%, based on preliminary studies of the Sr and Sr isotope geochemistry (Sonnenthal et al., 1997).

Background ^{36}Cl/Cl Ratios

The background ^{36}Cl/Cl ratio is considered to be that which has not been affected by the recent increase in the ^{36}Cl/Cl due to atmospheric testing of nuclear weapons. We can predict a general background value for the ^{36}Cl/Cl ratio; however, the possibility for localized mixing of transient bomb-pulse ^{36}Cl/Cl -bearing waters with matrix pore waters could result in locally high values at a scale of less than a meter that a large-scale continuum model may not be able to capture. In addition, fast path flow of waters carrying a bomb-pulse signature may last over very short periods (certainly less than a few years) which cannot be addressed using steady-state infiltration boundary conditions. The chloride concentrations alone allow for a rough estimate as to the background ratios that may be observed, based on the UZ model flow fields. In the western section, under Yucca Ridge, the region along the drift is completely flushed by waters less than 10,000 years old, and therefore we should expect ^{36}Cl/Cl ratios around 500e-15. In the eastern part, there are large concentration differences in matrix and fracture pore waters and we would expect a range of values between 500e-15 and 1200e-15 (the approximate maximum value during the last glacial period). If unambiguous bomb-pulse ratios are discovered by sampling in the E-W cross drift, any elevated background values nearby cannot be considered as reliable estimates of the possible ages of these waters. In these cases, other bomb-pulse isotopes (such as tritium) should be measured so that the distinction between a bomb-pulse component and a proportion of higher ratio Pleistocene water can be made. Using the formulation described by Equations 4-4.1 and 4-4.2, the background ^{36}Cl/Cl ratios have been calculated for matrix and fractures along the cross-drift (Figure 4-4.7), and illustrate the behavior descibed above.

Bomb-Pulse ^{36}Cl/Cl Ratios

Based on the geology along the East-West Cross Drift, bomb-pulse ^{36}Cl/Cl is likely to occur at the Sundance fault, a northwest-striking fault zone, and the surrounding area, where bomb-pulse ^{36}Cl/Cl has already been found at the level of the ESF (Levy et al., 1997). Using the same geologic information, bomb-pulse ^{36}Cl/Cl might also be encountered along the eastern edge and to the east of the Solitario Canyon fault zone where the alluvial cover is thin, the TSw is exposed directly at the surface, and the PTn unit is not present to act as a dampening unit. Based on the conceptual model of Fairley and Sonnenthal (1996), which states that fast pathway flow is likely to be linked to through-going structural features such as faults in areas of thin alluvial cover and high infiltration, bomb-pulse ^{36}Cl/Cl is not likely be encountered along the main channel of the Solitario Canyon where the alluvial cover is thickest. However, the magnitude and juxtaposition of offset units along the fault could allow some fast-flow to occur in this area. According to Fairley and Sonnenthal (1996), spatially localized occurrences of bomb-pulse ^{36}Cl/Cl are more indicative of rapidly transient infiltration pulses than long-term steady-state infiltration. As a result, transient flow behavior may be important because the PTn hydrogeologic unit is present to act as a dampening unit, and this transient flow is not captured by a steady state model. Bomb-pulse ^{36}Cl/Cl could also be expected at other locations along the East-West Cross Drift where alluvial cover is thin, infiltration is high, and through-going features exist. As in the region adjacent to the Sundance Fault, the presence of large subhorizontal cooling joints in the TSw middle nonlithophysal unit could result in a spread of bomb-pulse ratios around faults.

5.0 Summary and Conclusions

Ambient conditions, including pneumatic, moisture, thermal, and geochemical distributions and variations, were predicted along the East-West Cross Drift. Values of spatially-distributed predictions are provided at 50 meter intervals along the drift beginning at Station 0+00 in Appendix B. Predictions are summarized as follows:

1. Matrix saturations predicted along the drift with the dual-k model ranged from 0.66 to 0.92 and fracture saturations ranged from about 0.04 to 0.12. These saturation values indicate that perched water is unlikely to be intersected during drift excavation. Matrix water potentials ranged from -150 to -600 kPa for the base case infiltration scenario, from approximately -100 to -450 kPa for the infiltration multiplied by three scenario, and from approximately -300 to -700 kPa for the infiltration divided by three scenario.
2. Increased and decreased infiltration (by a factor of three) resulted in a 0.03 to 0.04 change in matrix saturations.
3. Predicted saturations were lower at the east end of the drift where infiltration rates are expected to be lower.
4. Some uncertainty is expected in all predictions made near the Solitario Canyon Fault zone. This uncertainty occurs because the spatial discretization of the UZ model grid may not adequately capture local heterogeneities along the fault zone that could impact prediction results.
5. Some uncertainty in model predictions may also occur near the Sundance Fault. This uncertainty could occur because this fault is expected to be intersected by the East-West Cross Drift, but is not incorporated into the model grid. As a result, local features such as offset in cooling joints, brecciation or zones of intense fracturing may exist near the fault that have not been considered by the model.
6. Another source of uncertainty in model predictions exists where the East-West Cross Drift is expected to pass through the lower non-lithophysal unit of the TSw between Stations 23+60 and 25+55 just east of the Solitario Canyon Fault. This uncertainty could occur because the 3-D UZ site-scale model is too coarse to capture all the lithostratigraphic layers expected along the cross-section at this location. As a result, some discrepancy is expected between observations and predictions at this location. In particular, saturations could be expected to be higher by 0.05 to 0.10 and water potentials could vary by -250 kPa.
7. Percolation fluxes predicted from the base-case infiltration scenario ranged from 0 to 17 mm/yr.
8. Simulated steady-state gas pressures ranged from 88.0 to 88.5 kPa. Field observations are expected to vary by as much as 2 kPa due to transient daily and seasonal changes that are not captured in a steady-state model. The impact of drift excavation on expected gas pressures is not considered.
9. Predicted temperatures ranged from about 22 to 25 degrees Celsius, with lower temperatures below the ridge top and near the Solitario Canyon Fault along the western portion of the drift.
10. Significant uncertainty exists in temperature predictions due to uncertainty in infiltration rates applied as surface boundary conditions and also due to the range of variability expected in specified surface and bottom boundary conditions.
11. Chloride concentrations should be in the range of about 10 to 30 mg/liter under the repository block, with higher concentrations near the Solitario Canyon Fault and on the east side near the North Ramp.

12. Strontium concentrations should be in the range of about 0.05 to 0.3 mg/liter under the repository block, with higher concentrations (up to about 1 mg/liter) on the western and eastern boundaries.
13. Background ^{36}Cl/Cl ratios are likely to be near modern values (500e-15) and more uniform under Yucca Ridge, and more variable to the east, where lower infiltration and incomplete equilibration between modern water in fractures and matrix pore waters is likely.
14. Bomb-pulse ^{36}Cl/Cl values may be found along the Sundance Fault, near fractures around the fault, and near other structural discontinuities below regions of high infiltration and areas of runoff.

The computer software used in the model calibrations and simulations in this report are Q. All data used in the report are Q, except the borehole temperature data which used qualified (Rousseau et al., 1996) and non-qualified data (Sass et al., 1988). However, this non-Q temperature data agrees with the Q borehole temperature data at higher elevations, so it can be considered as corroborating evidence for the temperature simulations at Yucca Mountain. Based on this assumption, all model results, predictions and conclusions presented in this report are Q.

6.0 Acknowledgments

The authors would like to thank H. H. Liu and A. K. Mishra for their careful and critical technical review of this report. Special thanks are also due to V. Fissekidou for conducting an internal QA review of the document.

This work was supported by the Director, Office of Civilian Radioactive Waste Management, U.S. Department of Energy, through a Memorandum Purchase Order EA9013MC5X between TRW Environmental Safety Systems, Inc. and Ernest Orlando Lawrence Berkeley National Laboratory, under Contract No. DE-AC03-76SF00098.

7.0 References (with project data tracking and accession numbers where available)

Ahlers, C.F.; Bandurraga, T.M.; Bodvarsson, G.S.; Chen, G.; Finsterle, S.; and Wu, Y.S. 1995a. *Summary of Model Calibration and Sensitivity Studies Using the LBNL/USGS Three-Dimensional Unsaturated-Zone Site-Scale Model.* Yucca Mountain Project Milestone 3GLM107M. Berkeley, California: Lawrence Berkeley National Laboratory. MOL19960208.0091-0097, LB092995312293.001 (Non-Q).

Ahlers, C.F.; Bandurraga, T.M.; Bodvarsson, G.S.; Chen, G.; Finsterle, S.; and Wu, Y.S. 1995b. *Performance Analysis of the LBNL/USGS Three-Dimensional Unsaturated-Zone Site-Scale Model.* Yucca Mountain Project Milestone 3GLM105M. Berkeley, California: Lawrence Berkeley National Laboratory. MOL19970116.0146.

Bandurraga, T.M. 1996. "Geological Model Development and Vertical Layering Scheme for the Numerical Grid." Chapter 2 of *Development and Calibration of the Three-Dimensional Site-Scale Unsaturated-Zone Model of Yucca Mountain, Nevada*, edited by G.S. Bodvarsson and M. Bandurraga. Yucca Mountain Site Characterization Project Milestone OBO2, Report LBNL-39315. Berkeley, California: Lawrence Berkeley National Laboratory. MOY-970317-04, LB960800831229.001, LB960800831229.002.

Bandurraga, T.M. and G.S. Bodvarsson, 1997. "Calibrating Matrix and Fracture Properties using Inverse Modeling." Chapter 6 OF "*The Site-Scale Unsaturated Zone Model of Yucca Mountain, Nevada, for the Viability Assessment*", Yucca Mountain Site Characterization Project Report, Bodvarsson, G.S., T.M. Bandurraga, and Yu-Shu Wu, eds., LBNL-40376, UC-814, Lawrence Berkeley National Laboratory, Berkeley, CA.

Bandurraga, T.M.; Wu, Y.S.; Ritcey, A.C.; Sonnenthal, E.; Ahlers, C.F.; Haukwa, C.; and Bodvarsson, G.S. 1997. *UZ Site-Scale Model Calibration, FY97.* Lawrence Berkeley National Laboratory Level 4 Milestone SP924UDM4, Yucca Mountain Site Characterization Report. Berkeley, California: Lawrence Berkeley National Laboratory. LB970301233129.001

Bodvarsson, G.S. and Bandurraga, T.M., 1996. Chapter 2 of *Development and Calibration of the Three-Dimensional Site-Scale Unsaturated-Zone Model of Yucca Mountain, Nevada.* Yucca Mountain Project Milestone SP24UFM4, Report LBNL-39315. Berkeley, California: Lawrence Berkeley National Laboratory. MOL: 199707010692, LB960800831229.001, LB960800831229.002

Bodvarsson, G.S., T.M. Bandurraga, and Yu-Shu Wu, eds., 1997. "*The Site-Scale Unsaturated Zone Model of Yucca Mountain, Nevada, for the Viability Assessment*", Yucca Mountain Site Characterization Project Report, LBNL-40376, UC-814, Lawrence Berkeley National Laboratory, Berkeley, CA.

Buesch, D.C.; Spengler, R.W.; Moyer, T.C.; and Geslin, J.K. 1995. *Nomenclature and Macroscopic Identification of Lithostratigraphic Units of the Paintbrush Group Exposed at Yucca Mountain, Nevada*. U.S. Geol. Surv. Open File Report 94-469. Denver, Colorado: U.S. Geological Survey. MOL19970205.0059, GS931208312421l.049 (Q).

Clayton, R.W., W.P. Zelinski, and C.A. Rautman, 1997. "ISM2.0: A 3-D Geologic Framework and Integrated Site Model of Yucca Mountain" Management and Operating Contractor, Las Vegas, NV, Rev. 00.

Doughty, C. and Bodvarsson, G.S. 1996. "Investigation of Conceptual and Numerical Approaches for Evaluating Gas, Moisture, Heat, and Chemical Transport." Chapter 6 of *Development and Calibration of the Three-Dimensional Site-Scale Unsaturated-Zone Model of Yucca Mountain, Nevada*, edited by G.S. Bodvarsson and M. Bandurraga, Yucca Mountain Site Characterization Project Milestone OBO2, Lawrence Berkeley National Laboratory, Berkeley, CA. MOL 199707010692, LB960800831229.001, LB960800831229.002.

Doughty, C. and Bodvarsson, G.S. 1997. "Investigation of Conceptual and Numerical Approaches for Evaluating Moisture Flow and Chemical Transport." Chapter 5 of *The Site-Scale Unsaturated Zone Model of Yucca Mountain, Nevada, for the Viability Assessment*, edited by G.S. Bodvarsson, T.M. Bandurraga, and Y.S. Wu. Yucca Mountain Project Milestone Report SP24UFM4; LBNL-40376. Berkeley, California: Lawrence Berkeley National Laboratory. LB9706001233129.001.

Fabryka-Martin, J., 1998. "Chlorine-36 and Chloride Studies at Yucca Mountain", Presentation, Chlorine-36 Peer Review, Las Vegas, NV.

Fairley, J. and Sonnenthal, E. 1996. "Preliminary Conceptual Model of Flow Pathways Based on Cl-36 and Other Environmental Isotopes." Chapter 10 of *Development and Calibration of the Three-Dimensional Site-scale Unsaturated-zone Model of Yucca Mountain, Nevada*, edited by G.S. Bodvarsson and M. Bandurraga. Yucca Mountain Site Characterization Project Milestone OBO2, Report LBNL-39315. Berkeley, California: Lawrence Berkeley National Laboratory. MOL199707010692, LB960800831229.001, LB960800831229.002.

Finsterle S. 1993. *ITOUGH2 User's Guide*. Version 2.2. Report LBNL-34581, UC-600. Berkeley, California: Lawrence Berkeley National Laboratory. MOL19941026.0075.

Flint, A.L.; Hevesi, J.A.; and Flint, L.E. 1996. (Unpublished) *Conceptual and Numerical Model of Infiltration for the Yucca Mountain Area, Nevada.* Milestone Report 3GU1623M, U. S. Geol. Surv. Water Resour. Invest. Rep. Denver, Colorado: Submitted for publication as a Water-Resources Investigations Report, U.S. Geological Survey. MOL19970409.0087, GS960908312211.003.

Fridrich, C.J.; Dudley, W.W., Jr.; and Stuckless, J.S. 1994. "Hydrogeologic Analysis of the Saturated-zone Groundwater System, under Yucca Mountain, Nevada." *Journal of Hydrology, 154*, 133-168. GS920708318325.001, MOL19940811.0102.

Haukwa, C. and Wu, Y.S. 1997. "Grid Generation and Analysis." Chapter 4 of *The Site-Scale Unsaturated Zone Model of Yucca Mountain, Nevada, for the Viability Assessment,* edited by G.S. Bodvarsson, T.M. Bandurraga, and Y.-S. Wu. Yucca Mountain Project Milestone Report SP24UFM4. Berkeley, California: Lawrence Berkeley National Laboratory. LB9706001233129.001.

Hinds, J.; Bandurraga, T.M.; Feighner, M.A.; and Wu, Y.S. 1997. "Geology of the Unsaturated Zone and the UZ Model." Chapter 3 of *The Site-Scale Unsaturated Zone Model of Yucca Mountain, Nevada, for the Viability Assessment*, edited by G.S. Bodvarsson, T.M. Bandurraga, and Y.S. Wu. LBNL-40376. Berkeley, California: Lawrence Berkeley National Laboratory. LB970601233129.001.

Ho, C.K., and N.D. Francis, 1997. Memo from authors to distribution, Correction to the Base-Case Thermal Properties for TSPA-VA Modeling, SNL.

International Formulation Committee, 1967. *A Formulation of the Thermodynamic Properties of Ordinary Water Substance.* Dusseldorf, Germany: IFC Secretariat. NNA19890918.0501.

Kwicklis, E.M., G.S. Bodvarsson and A.L. Flint, DRAFT 1996. "A Conceptual Model of the Unsaturated Zone Flow and Transport, Yucca Mountain, Nevada,", WRI Report 96-XXX, Denver, CO.

Lu, N., and E.M. Kwicklis, 1995. A Preliminary, Two-Dimensional Numerical Model for Gas Circulation Around UZ-6s, Yucca Mountain, Nevada, U.S. Geological Survey, Lakewood, CO.

Levy, S.S.; Sweetkind, D.S.; Fabryka-Martin, J.T.; Dixon, P.R.; Roach, J.L.; Wolfberg, L.E.; Elmore, D.; and Sharma, P. 1997. *Investigations of Structural Controls and Mineralogic Associations of Chlorine-36 Fast Pathways in the ESF.* Yucca Mountain Project Milestone Report SP2301M4, LA-EES-1-TIP-97-004. Los Alamos, New Mexico: Los Alamos National Laboratory.

Moyer, T. C. and Geslin, J.K. 1995. *Lithostratigraphy of the Calico Hills Formation and Prow Pass Tuff (Crater Flat Group) at Yucca Mountain, Nevada.* U.S. Geol. Surv. Rep. OFR 94-460. Denver, Colorado: U.S. Geological Survey. GS940608314211.028 (Non-Q).

Oldenburg, C.M., and K. Pruess, 1995. "Dispersive transport dynamics in a strongly coupled groundwater-brine flow system" in Water Resources Research, Vol., 31, No., 2, pp. 289-302.

Potter, C.J., R.P. Dickerson and W.C. Day, 1995."Nature and Continuity of the Sundance Fault, Yucca Mountain, Nevada", USGS Administrative Report, Denver, CO.

Pruess, K. 1987. *TOUGH User's Guide.* Nuclear Regulatory Commission, Report NUREG/CR-4645; Report LBL-20700. Berkeley, California: Lawrence Berkeley National Laboratory. NNA19890315.0010.

Pruess K. 1991. *TOUGH2—A General Purpose Numerical Simulator for Multiphase Fluid and Heat Flow.* Report LBL-29400, UC-251, Berkeley, California: Lawrence Berkeley National Laboratory. NNA1940202.0088.

Pruess, K., A. Simmons, Y.S. Wu, and G. Moridis, 1996. TOUGH2 Software Qualification, Lawrence Berkeley National Laboratory Report LBL-38383, UC-814, Lawrence Berkeley National Laboratory , Berkeley, CA, ACCN: MOL19960610.0010.0020

Ritcey, A.C. Yu-Shu Wu, E. Sonnethal, C. Haukwa and G. S. Bodvarsson, 1998. Predictions of Ambient Conditions along the East-West Cross Drift using the 3-D UZ site-scale model, Lawrence Berkeley National Laboratory Milestone SP33AAM4, Berkeley, CA.

Rousseau, J.P.; Kwicklis, E.M.; and Gillies, D.C., eds., 1996 (In Press). *Hydrogeology of the Unsaturated Zone, North Ramp Area of the Exploratory Studies Facility, Yucca Mountain, Nevada,* USGS-WRIR-98-4050 Yucca Mountain Project Milestone Report 3GUP667M (formerly 3GUP431M). Submitted for publication as a Water-Resources Investigations Report, U.S. Geological Survey, Denver, Colorado.

Sass, J.H.; Lachenbruch, A.H.; Dudley, W.W., Jr.; Priest, S.S.; and Munroe, R.J. 1988. *Temperature, Thermal Conductivity and Heat Flow near Yucca Mountain, Nevada: Some Tectonic and Hydrologic Implications.* U.S. Geol. Surv. Open File Rep. 87-649. Denver, Colorado: U.S. Geological Survey. DE89 002697, NNA19890123.0010, GS950408318523.001 (Non-Q).

Sonnenthal, E.L. D.J. DePaulo and Bodvarsson, G.S.1997. "Modeling the Strontium Geochemistry and Isotopic Ratio in the Unsaturated Zone". Chapter 17 of *The Site-Scale Unsaturated Zone Model of Yucca Mountain, Nevada,* for the Viability Assessment, edited by G.S. Bodvarsson, T.M. Bandurraga, and Y.S. Wu. Yucca Mountain Site Characterization Project Milestone Report SP24UFM4; Report LBNL-40376. Berkeley, California: Lawrence Berkeley National Laboratory. LB970601233129.001.

Sonnenthal, E.L. and Bodvarsson, G.S.1997. "Modeling the Chloride Geochemistry in the Unsaturated Zone" Chapter 15 of *The Site-Scale Unsaturated Zone Model of Yucca Mountain, Nevada,* for the Viability Assessment, edited by G.S. Bodvarsson, T.M. Bandurraga, and Y.S. Wu. Yucca Mountain Site Characterization Project Milestone Report SP24UFM4; Report LBNL-40376. Berkeley, California: Lawrence Berkeley National Laboratory. LB970601233129.001.

Triay, I.R.; Meijer, A.; Conca, J.L.; Kung, K.S.; Rundberg, R.S.; and Streitelmeier, E.A. 1996. "Summary and Synthesis Report on Radionuclide Retardation for the Yucca Mountain Site Characterization Project." Milestone 3784M.

Tyler, S.W., J.B. Chapman, S.H. Conrad, D.P. Hammermeister, D.O. Blout, J.J. Miller, M.J. Sully, and J.M. Ginanni, 1996. Soil-Water Flux in the Southern Great Basin, United States: Temporal and Spatial Variations over the Last 120,000 Years, Water Resour. Res., *32* (6), 1481-1499,

TRW Environmental Safety Systems, Inc., 1998. CRWMS Management and Operating Contractor, ECRB Predictive Geotechnical Report-Volume I: Geotechnical Baseline Report, BABEA0000-01717-5705-00002, Revision 0, Las Vegas, NV.

Wu, Y.S.; Ahlers, C.F.; Fraser, P.; Simmons, A.; and Pruess, K. 1996. *Software Qualification of Selected TOUGH2 Modules.* Report LBNL-39490, UC-800. Berkeley, California: Lawrence Berkeley National Laboratory. MOL19970219.0100-0105.

Wu, Y.S.; Chen, G.; Haukwa, C.; and Bodvarsson, G.S. 1996a. "Three-Dimensional Model Calibration and Sensitivity Studies." Chapter 8 of *Development and Calibration of the Three-Dimensional Site-Scale Unsaturated-Zone Model of Yucca Mountain, Nevada,* edited by G.S. Bodvarsson and M. Bandurraga. Yucca Mountain Site Characterization Project Milestone OBO2. Berkeley, California: Lawrence Berkeley National Laboratory. MOL199707010692, LB960800831229.001, LB960800831229.002.

Wu, Y.S.; Ritcey, A.C.; Ahlers, C.F.; Haukwa, C.; Hinds, J.J.; Sonnenthal, E.L.; Mishra, A.K.; and Bodvarsson, G.S. 1997. *Providing Base Case Flow Fields for TSPA-VA: Evaluation of Uncertainty of Present Day Infiltration Rates Using the 3-D Site Scale UZ Flow Model.* Level 4 Milestone Report SLX01LB1, LB971100001254.001, MOL LB971100001254.001.

Wu, Y.S.; Ritcey, A.C.; Sonnenthal, E.L.; Bandurraga, T.M.; Haukwa, C.; Fairley, J.P.; Chen, G.; Li, J.H.; and Bodvarsson, G.S. 1997a. *Incorporation of Perched Water Data into the UZ Site-scale Model.* Yucca Mountain Project Milestone SP24UCM4. Berkeley, California: Lawrence Berkeley National Laboratory.

Yang, I.C., G.W. Rattray, and P. Yu. 1996. Interpretations of Chemical and Isotopic Data from Boreholes in the Unsaturated Zone at Yucca Mountain, Nevada. U.S. Geol. Surv. Water Resour. Invest. Rep. 96-4058. Denver, Colorado: U.S. Geological Survey. GS970108312271.001.

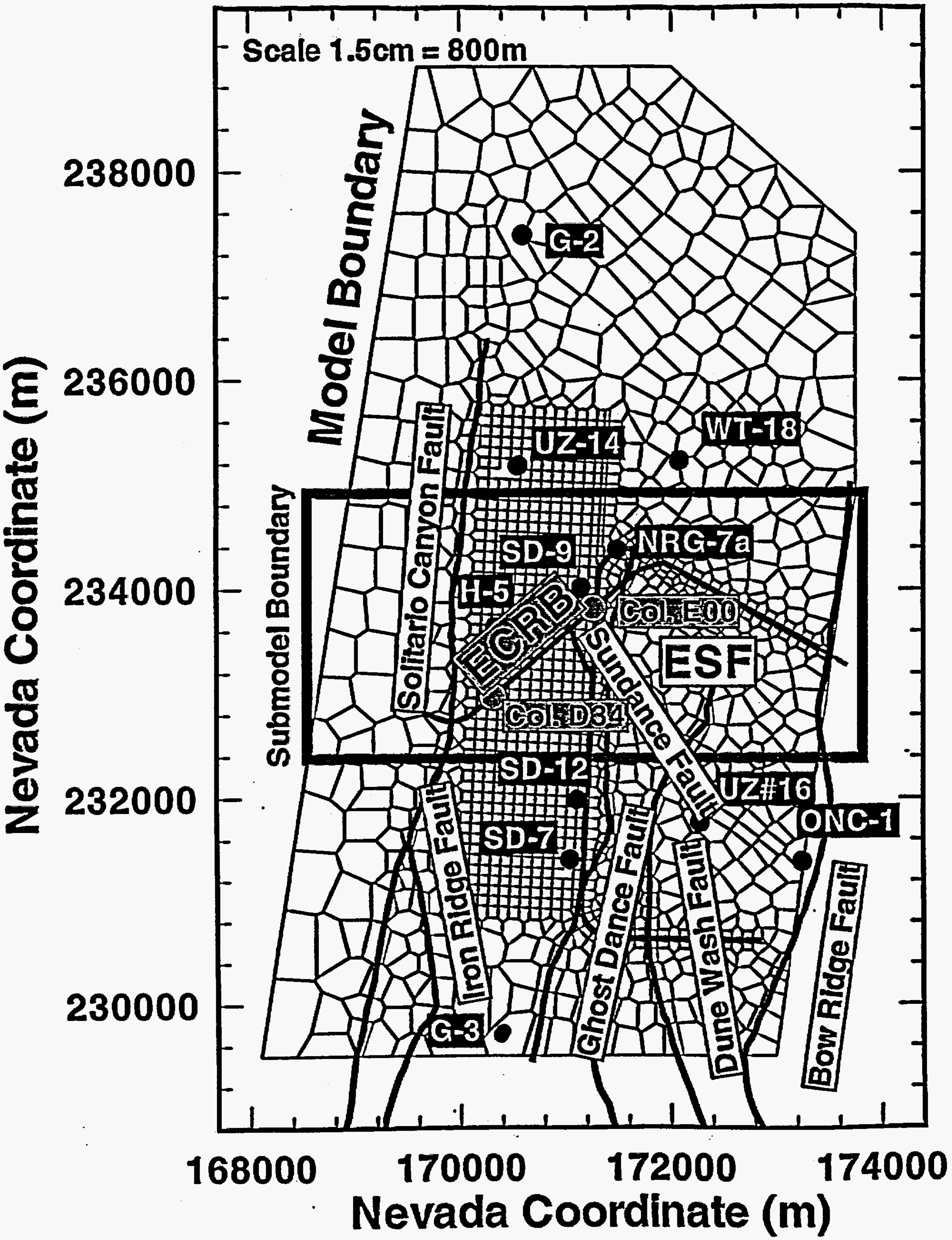

Figure 1.0-1 Plan view showing the model domain, grid, faults, the ESF, the East-West Cross Drift (designated here as the ECRB), the location of some boreholes, the ECM sub-model domain, and the location of two columns, #D34 and #E00 used to extract results.

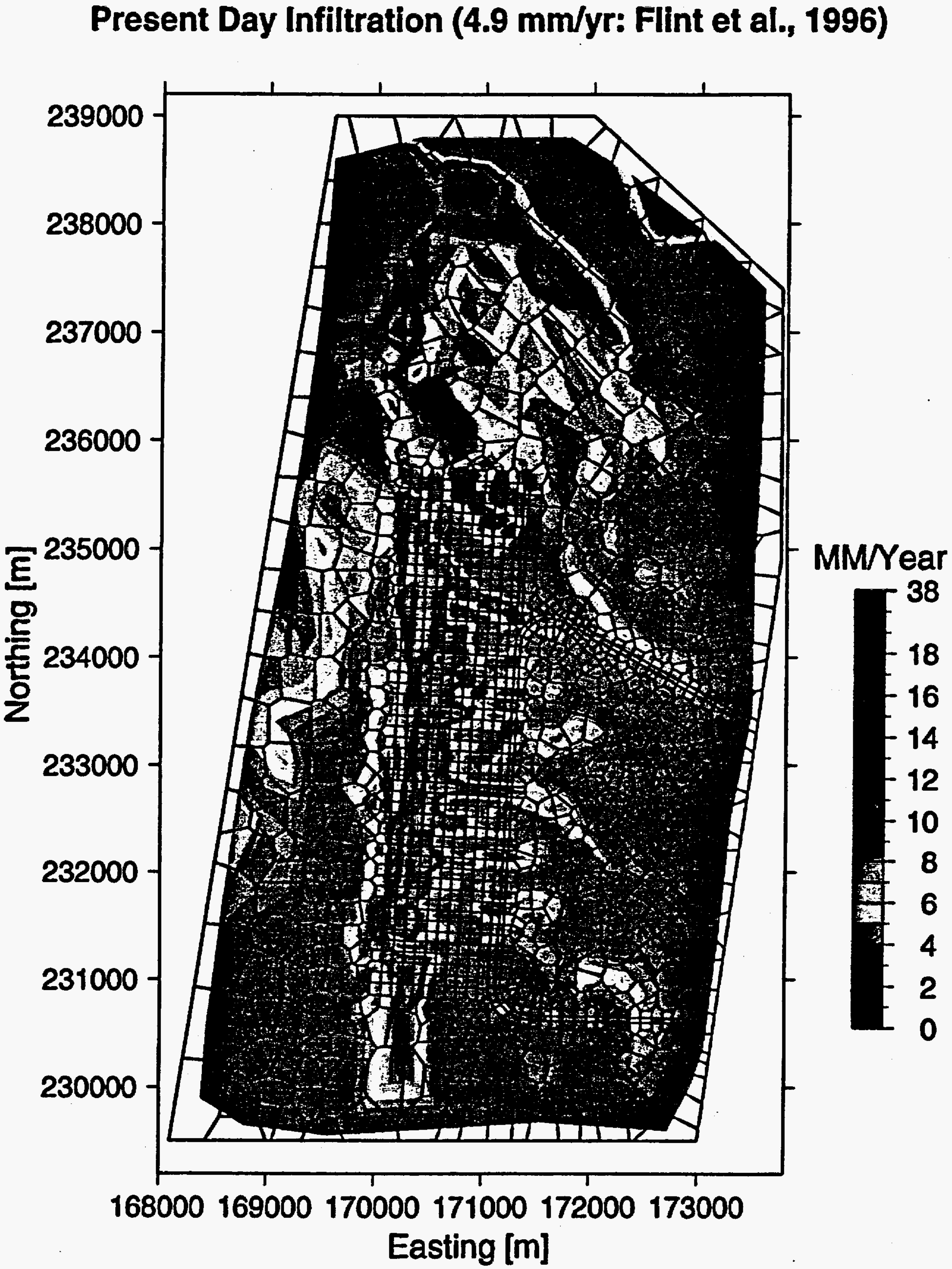

Figure 3.2-1 Plan view of the spatial distribution of net infiltration over Yucca Mountain in mm/yr (modified from Flint et al., 1996).

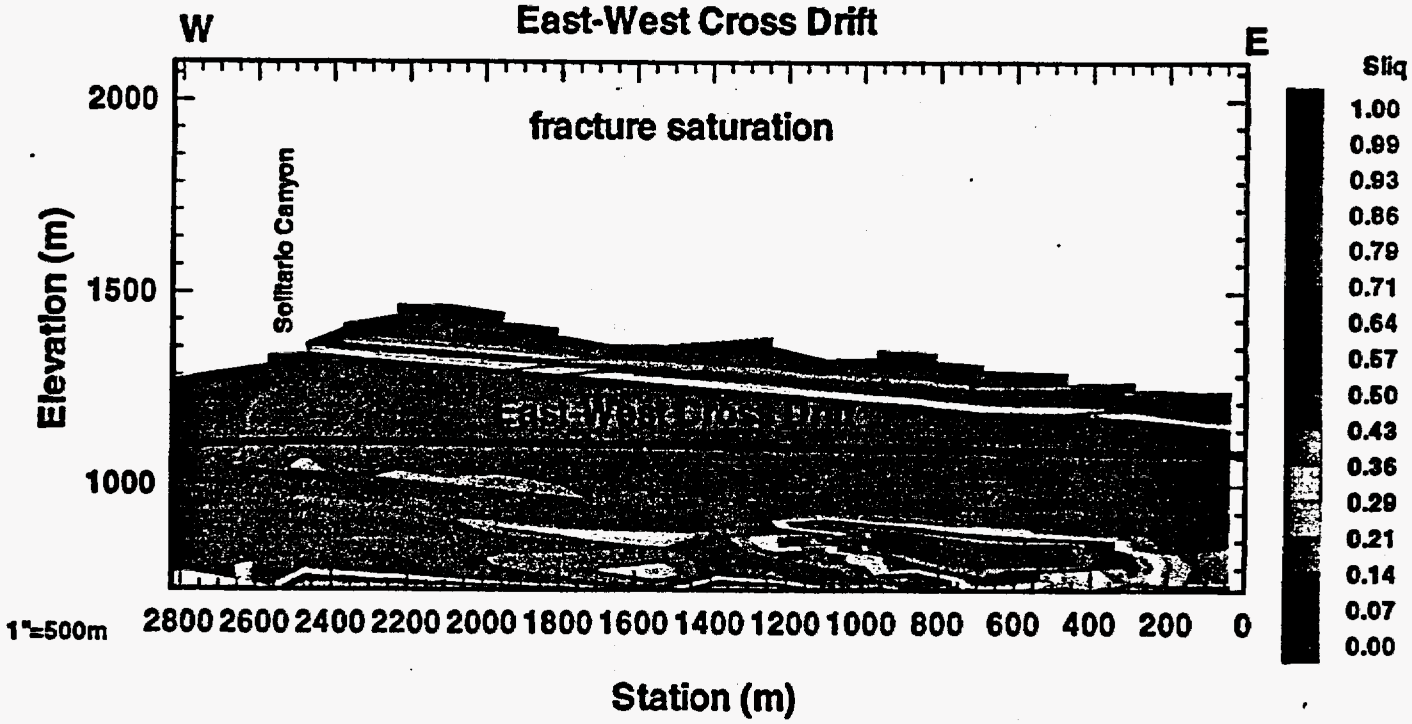

Figure 4.1-1 Modeled fracture saturations for the base-case infiltration scenario contoured along a 2-D cross section extracted from 3-D model results. Cross section is aligned along the East-West Cross Drift.

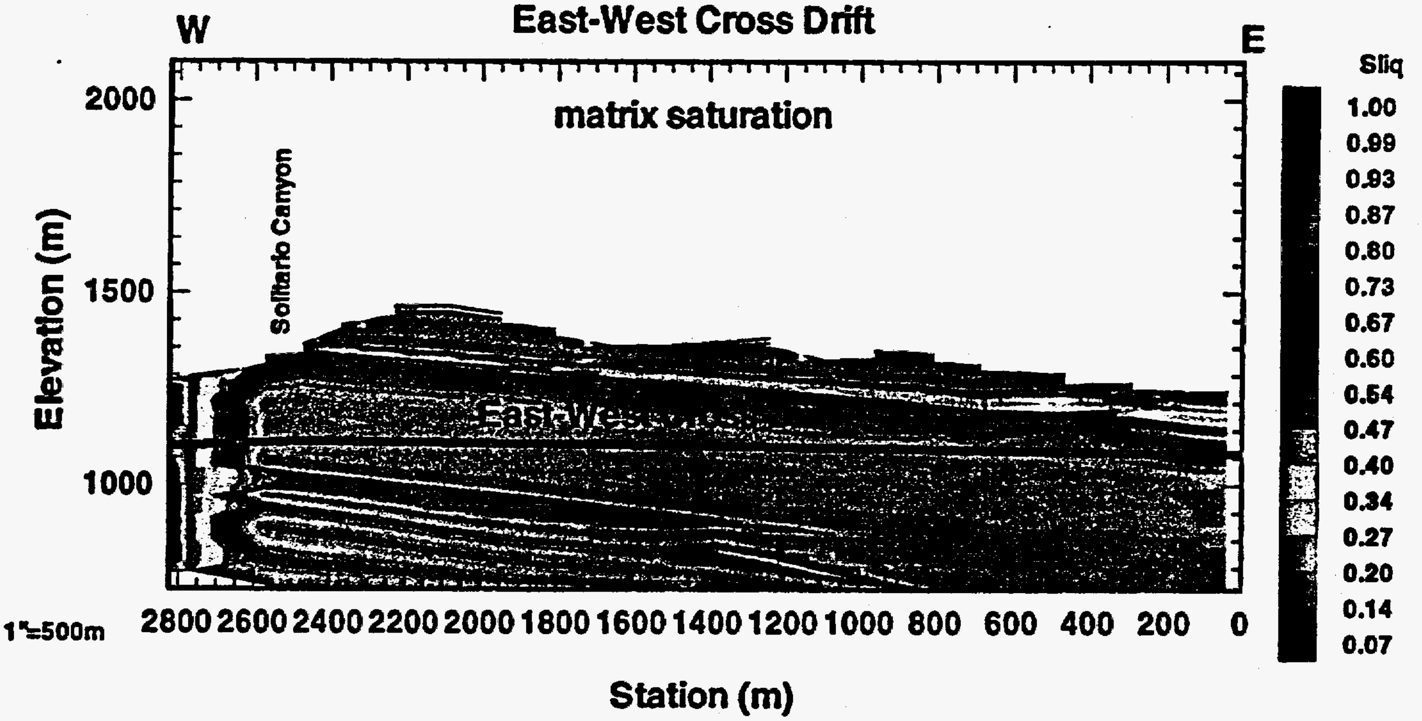

Figure 4.1-2 Modeled matrix saturations for the base-case infiltration scenario contoured along a 2-D cross section extracted from 3-D model results. Cross section is aligned along the East-West Cross Drift.

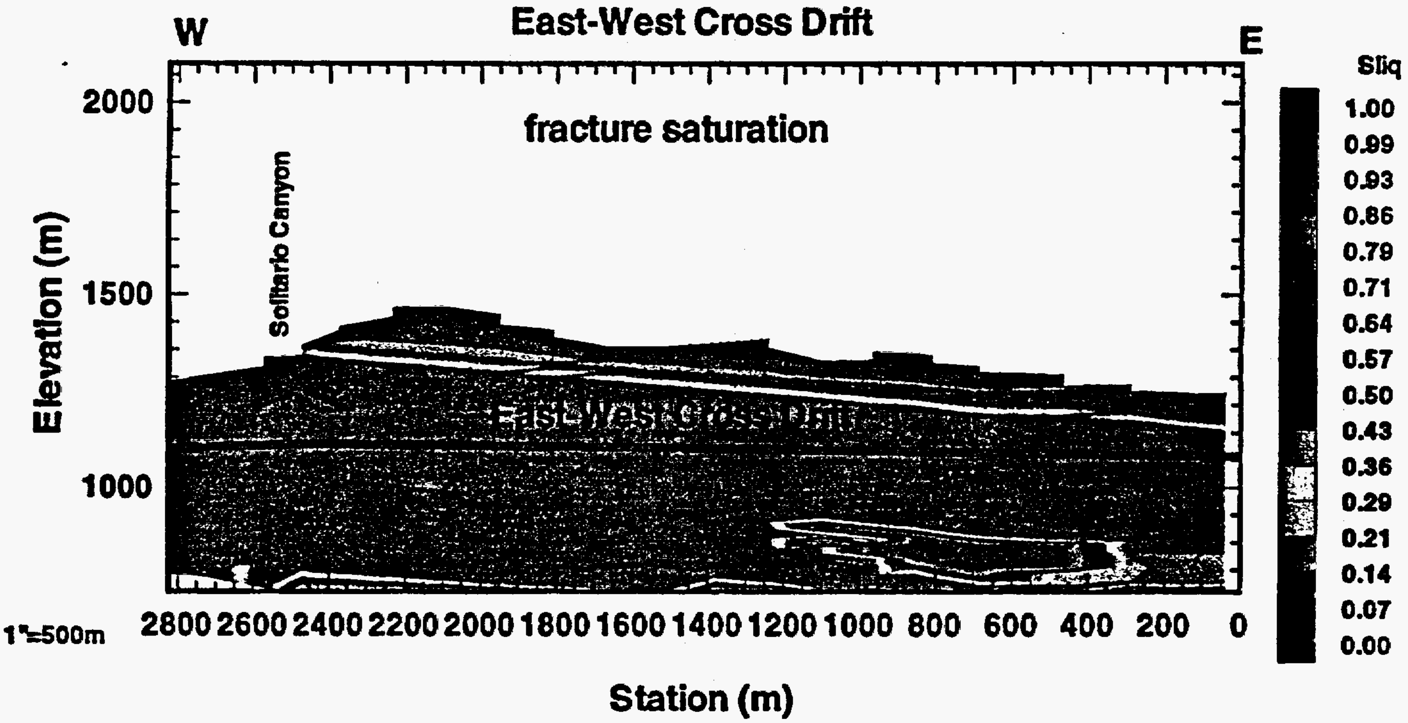

Figure 4.1-3 Modeled fracture saturations for the infiltration multiplied by 3 scenario contoured along a 2-D cross section extracted from 3-D model results. Cross section is aligned along the East-West Cross Drift.

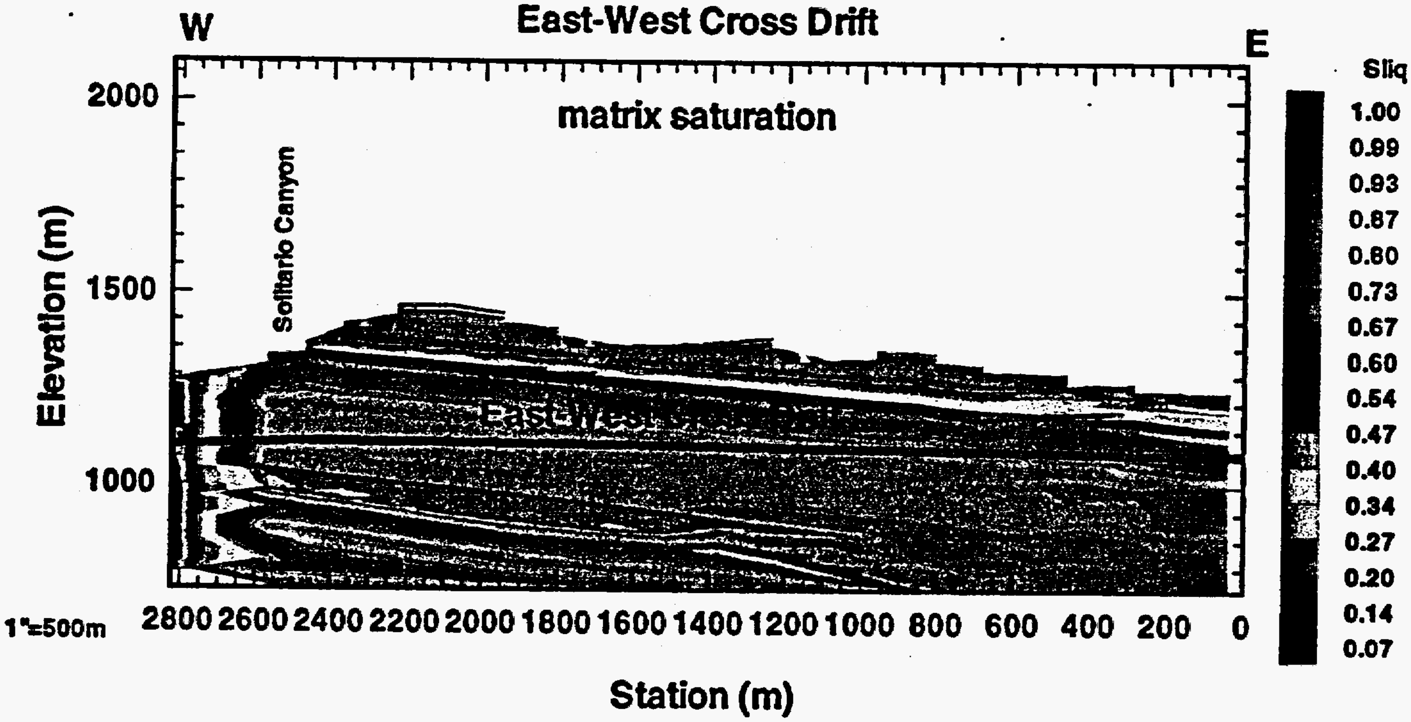

Figure 4.1-4 Modeled matrix saturations for the infiltration multiplied by 3 scenario contoured along a 2-D cross section extracted from 3-D model results. Cross section is aligned along the East-West Cross Drift.

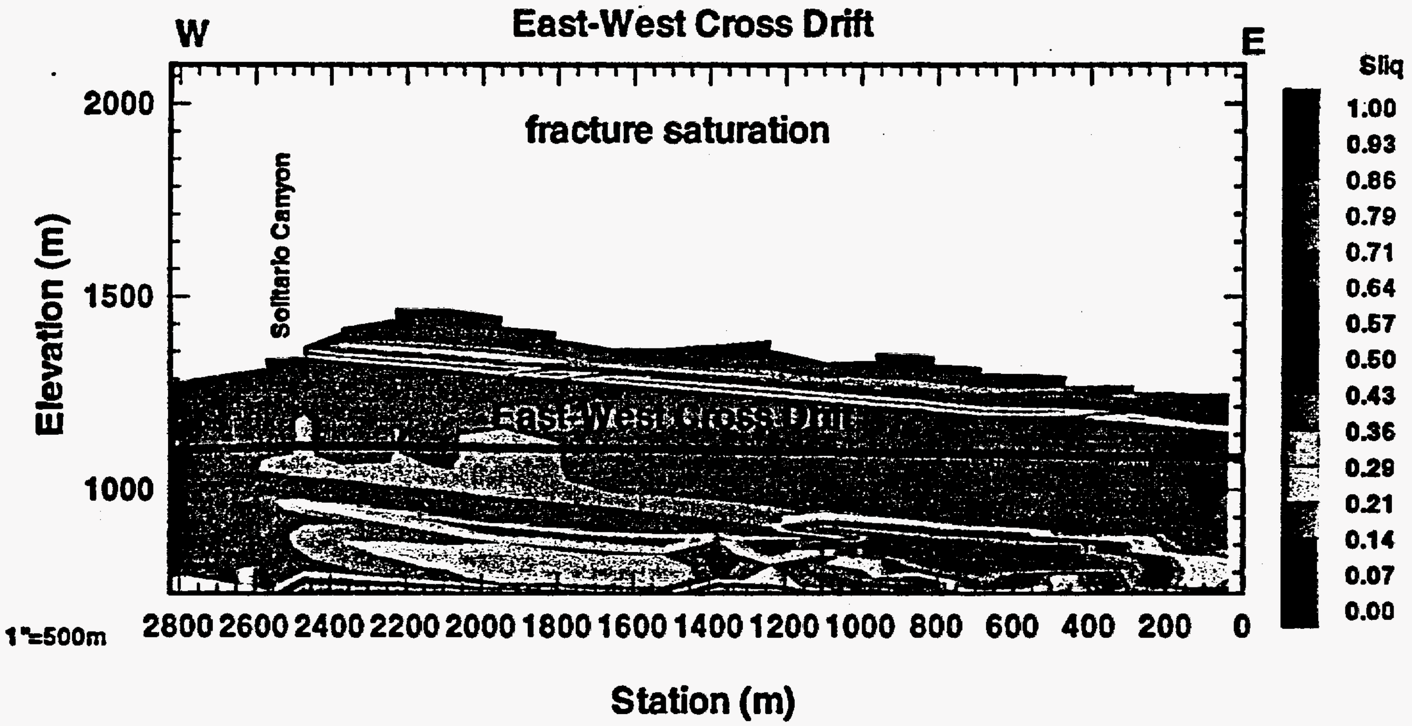

Figure 4.1-5 Modeled fracture saturations for the infiltration divided by 3 scenario contoured along a 2-D cross section extracted from 3-D model results. Cross section is aligned along the East-West Cross Drift.

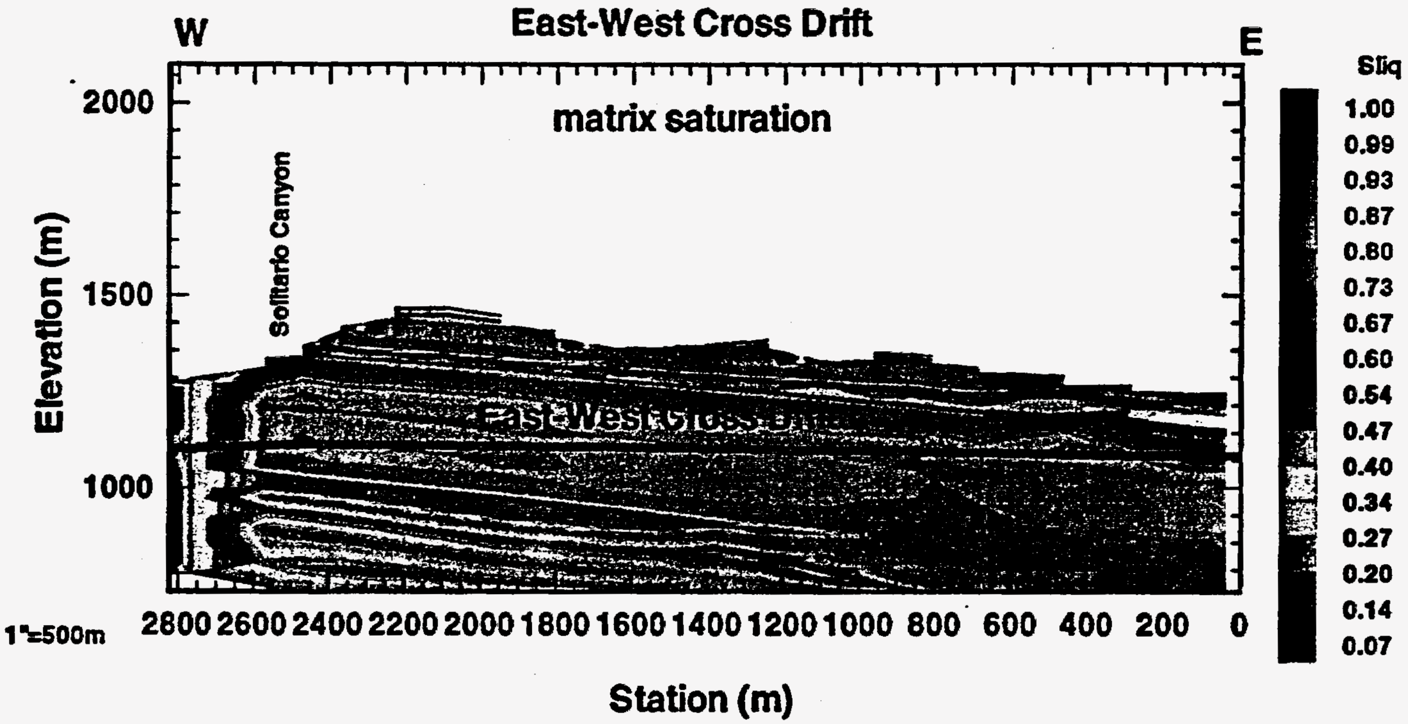

Figure 4.1-6 Modeled matrix saturations for the infiltration divided by 3 scenario contoured along a 2-D cross section extracted from 3-D model results. Cross section is aligned along the East-West Cross Drift.

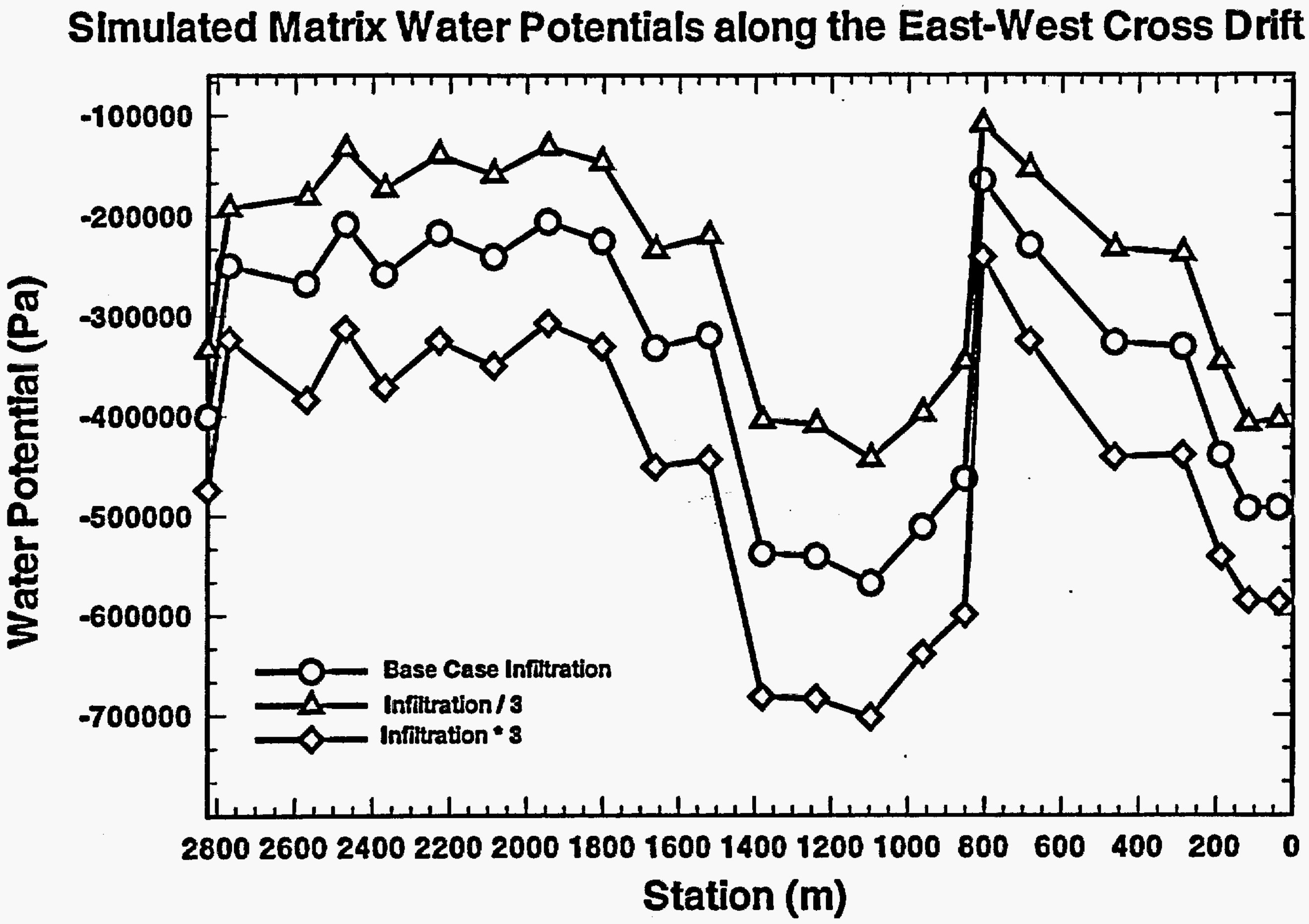

Figure 4.1-7 Simulated matrix water potentials along the East-West Cross Drift.

1"=500m

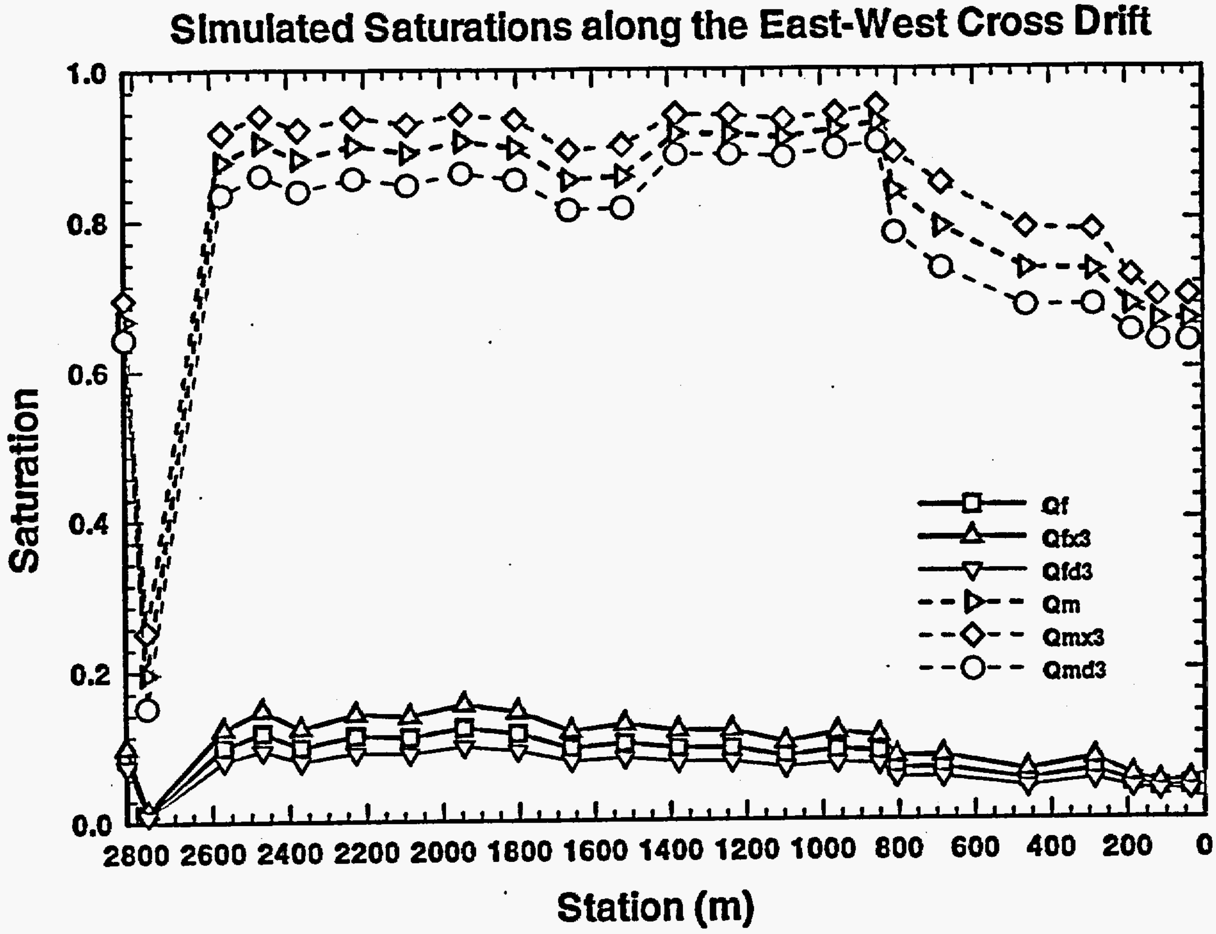

1"=500m

Figure 4.1-8 Modeled fracture and matrix saturations along the East-West Cross Drift. "Qf", "Qfd3" and "Qfx3" represent the fracture saturations for the base-case, the infiltration divided by three, and the infiltration multiplied by three scenarios, respectively. "Qm", "Qmd3" and "Qmx3" represent the matrix saturations for these three cases.

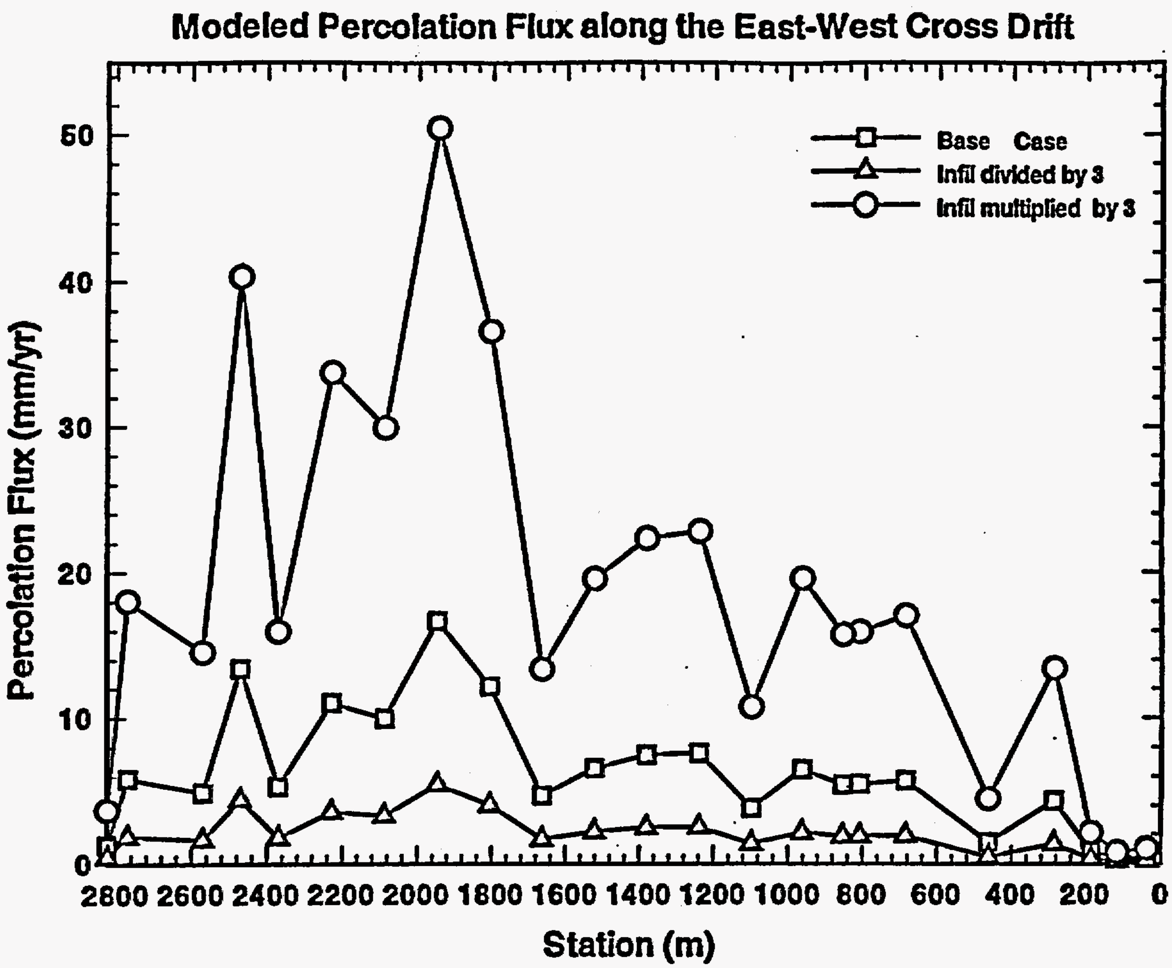

Figure 4.1-9 Simulated percolation fluxes along the East-West Cross Drift.

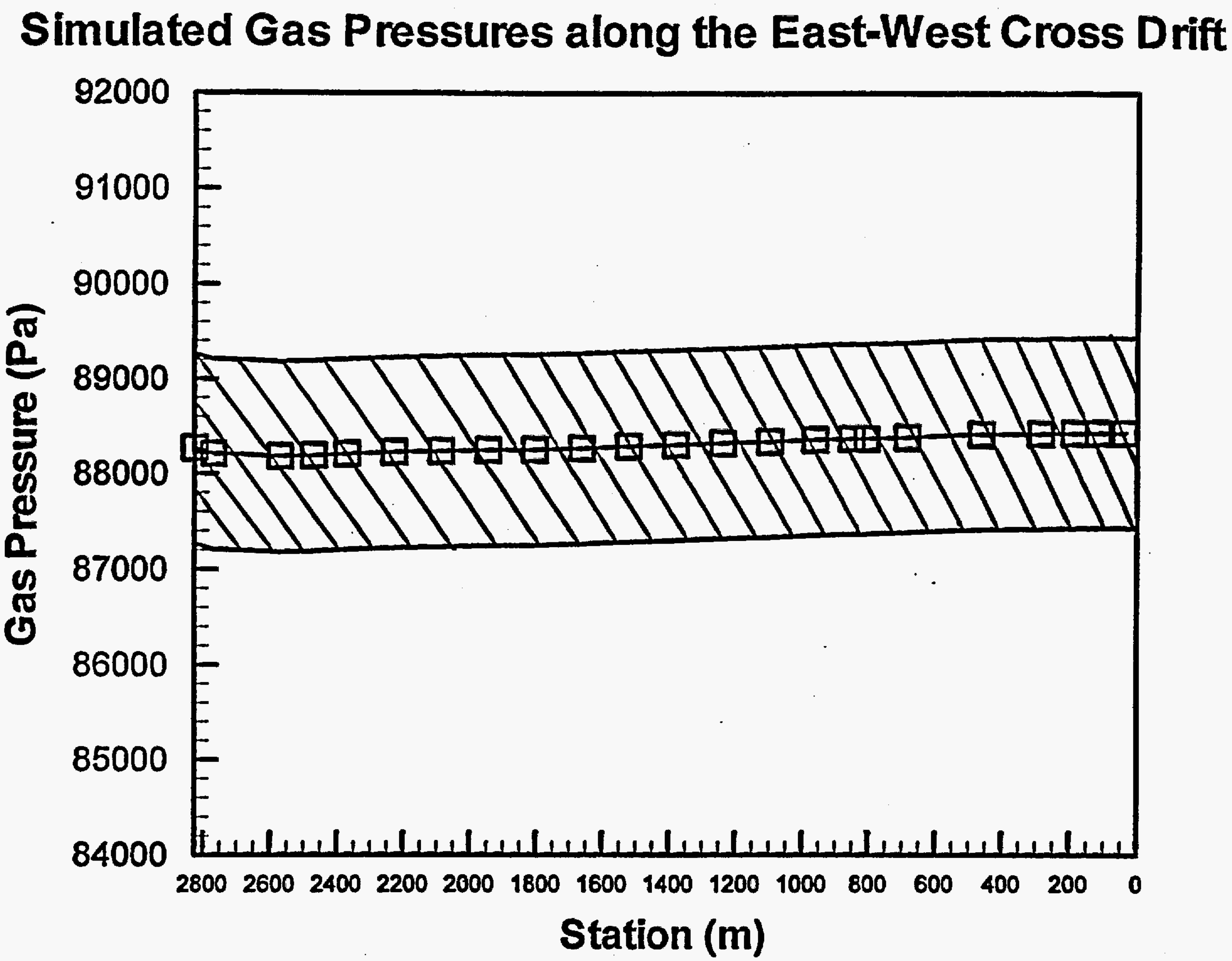

Figure 4.2-1 Simulated gas pressures along the East-West Cross Drift.

1"=500m

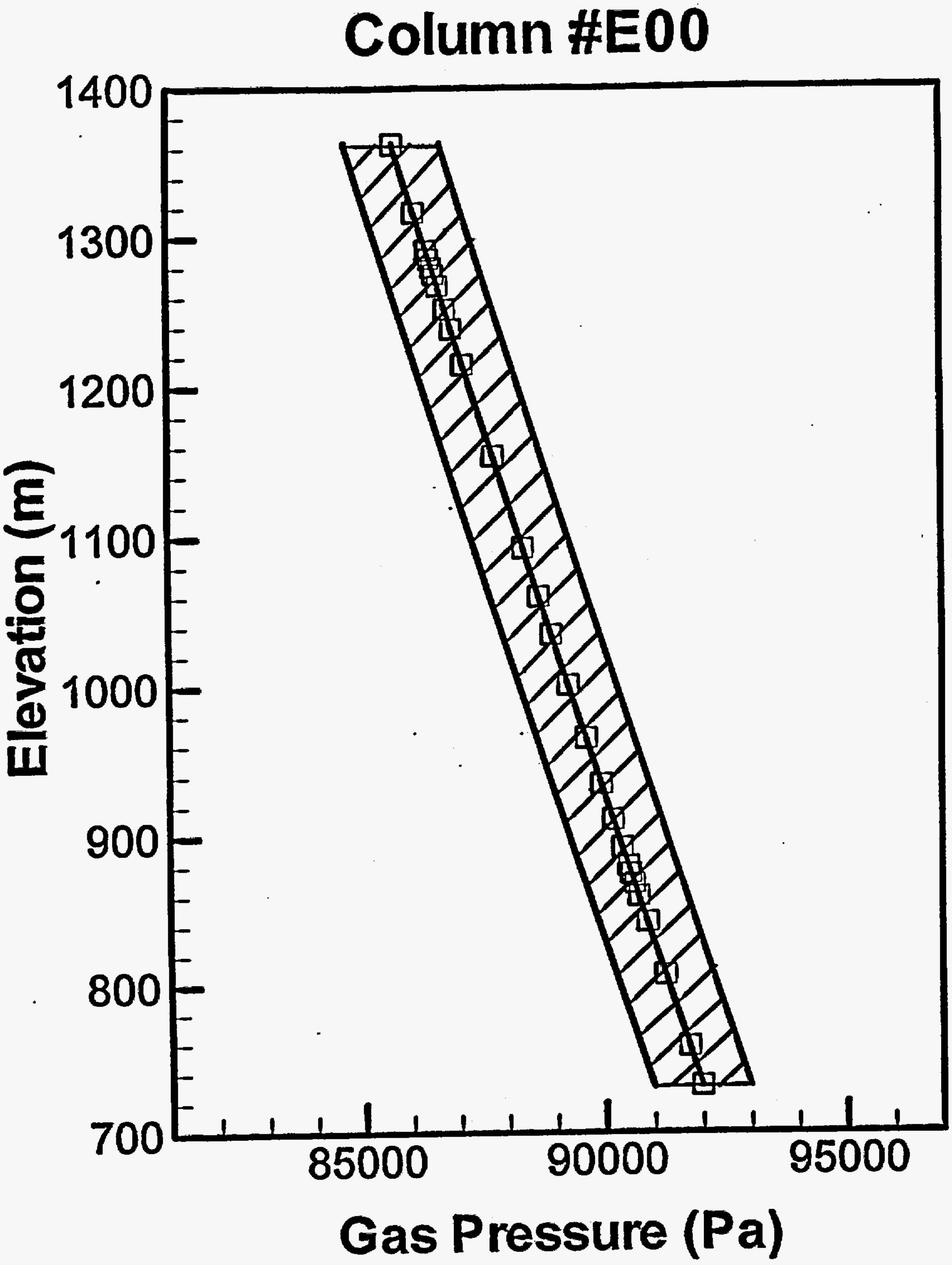

Figure 4.2-2 Simulated 1-D gas pressure profile along column E00 extracted from the 3-D ECM model results.

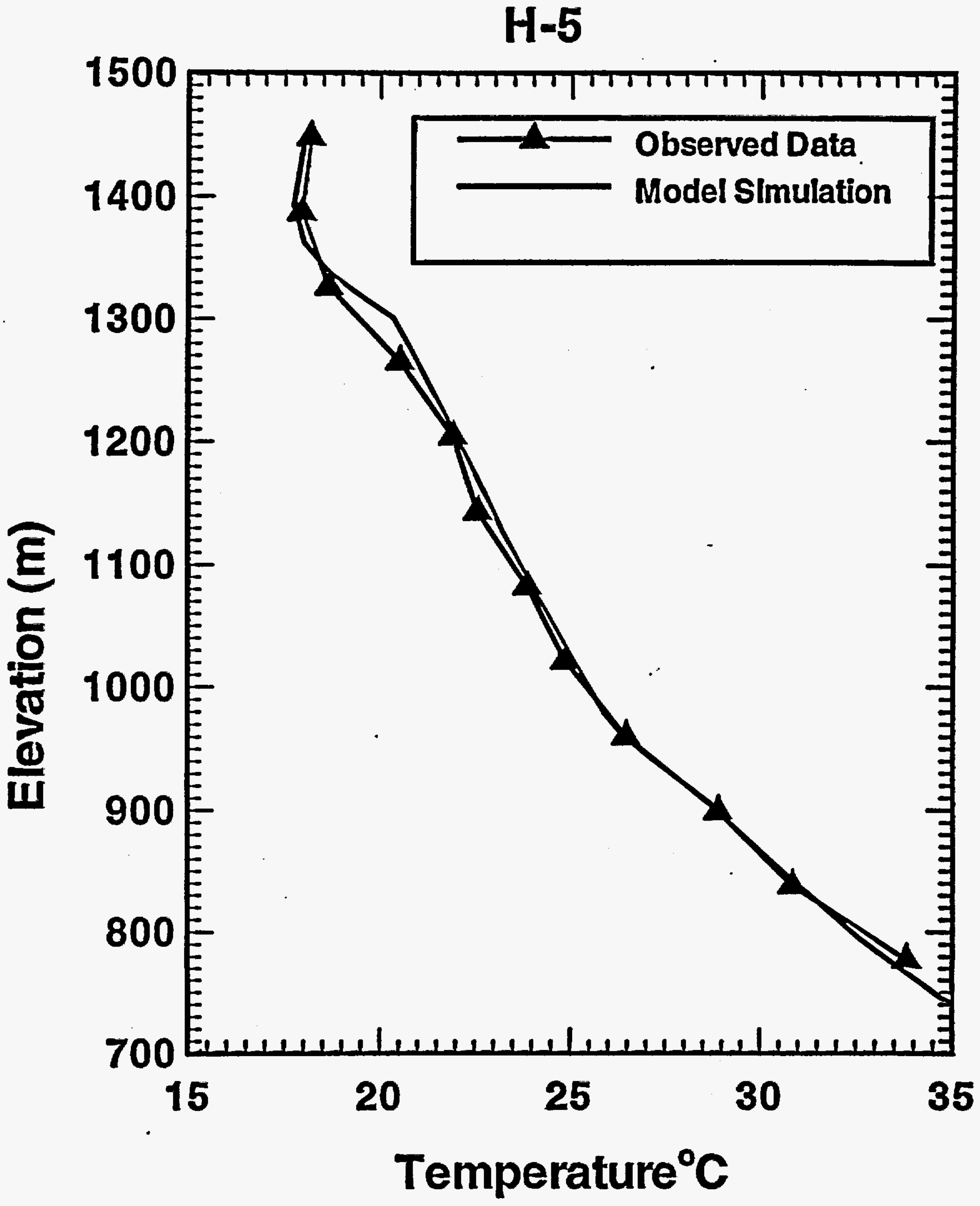

Figure 4.3-1 Comparison between an observed and modeled temperature profile at Borehole H-5.

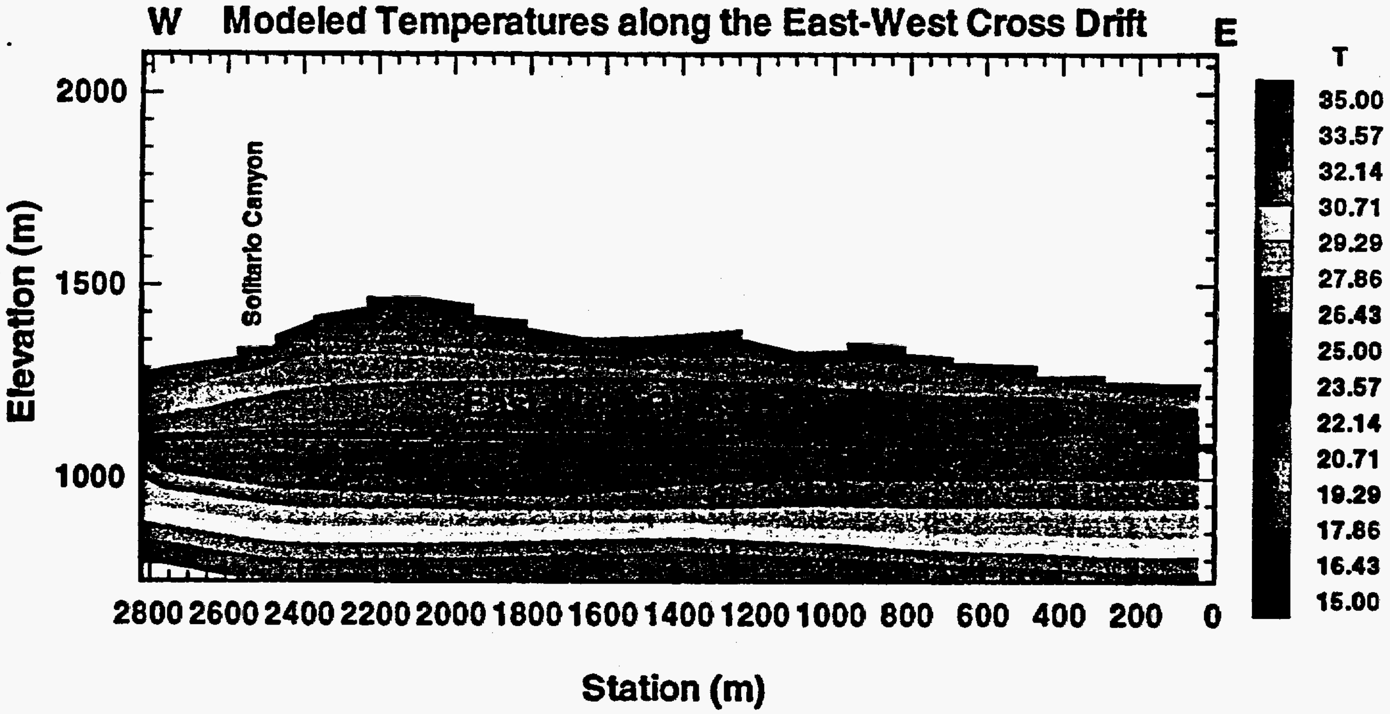

Figure 4.3-2 Modeled temperatures contoured along the East-West Cross Drift.

1"=500m

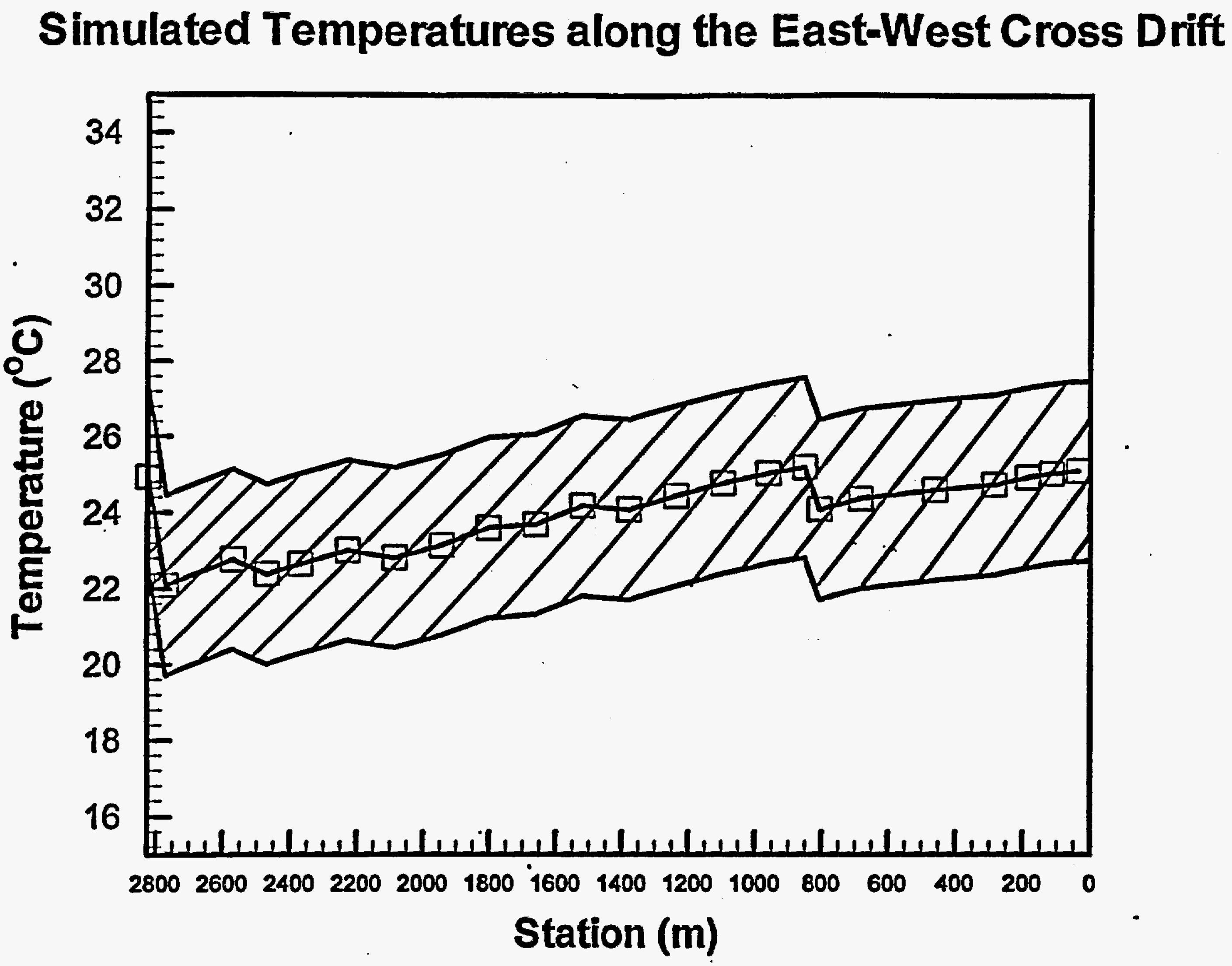

Figure 4.3-3 Simulated Temperatures along the East-West Cross Drift.

1"=500m

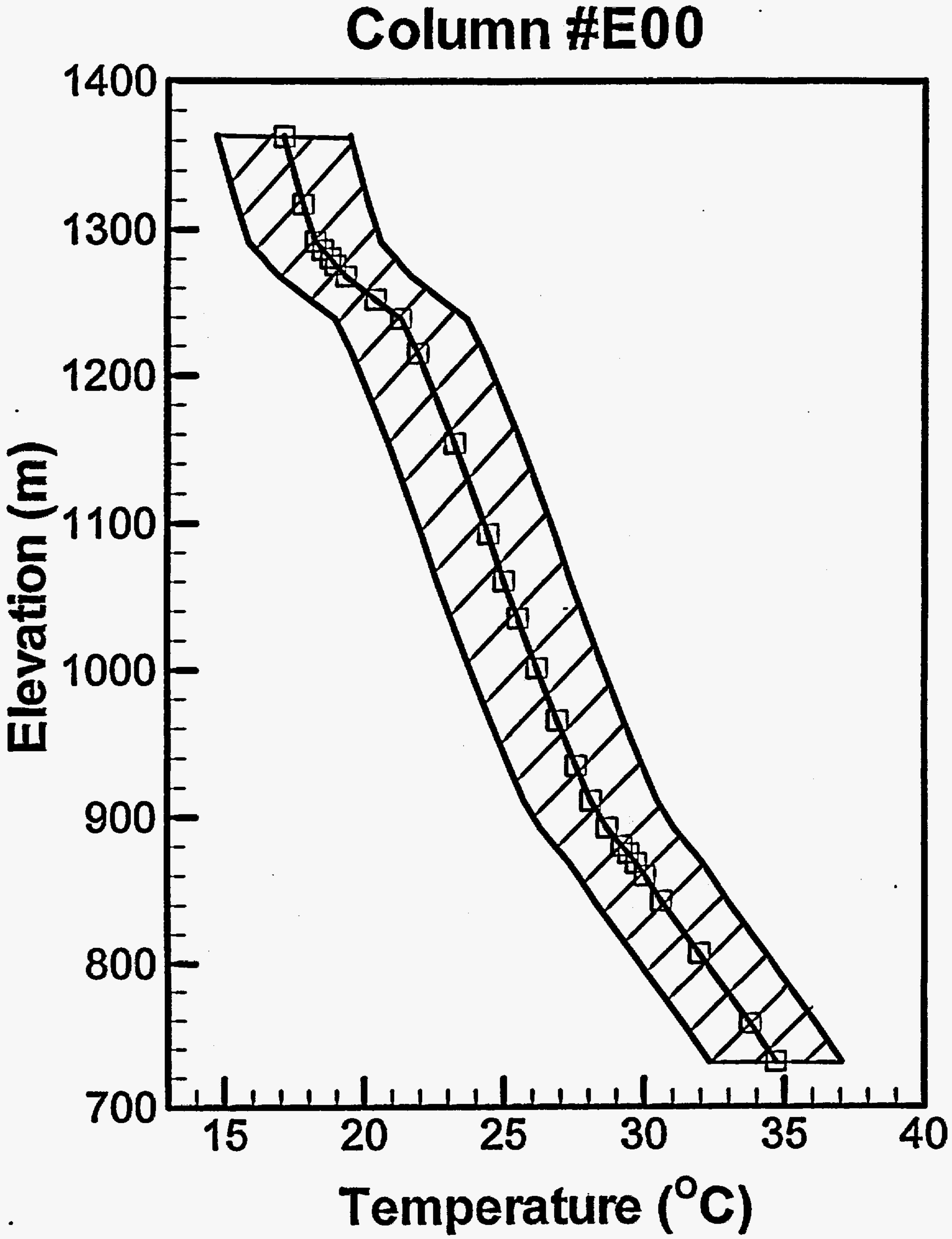

4.3-4 Simulated 1-D temperature profile along Column E00 extracted from 3-D model results.

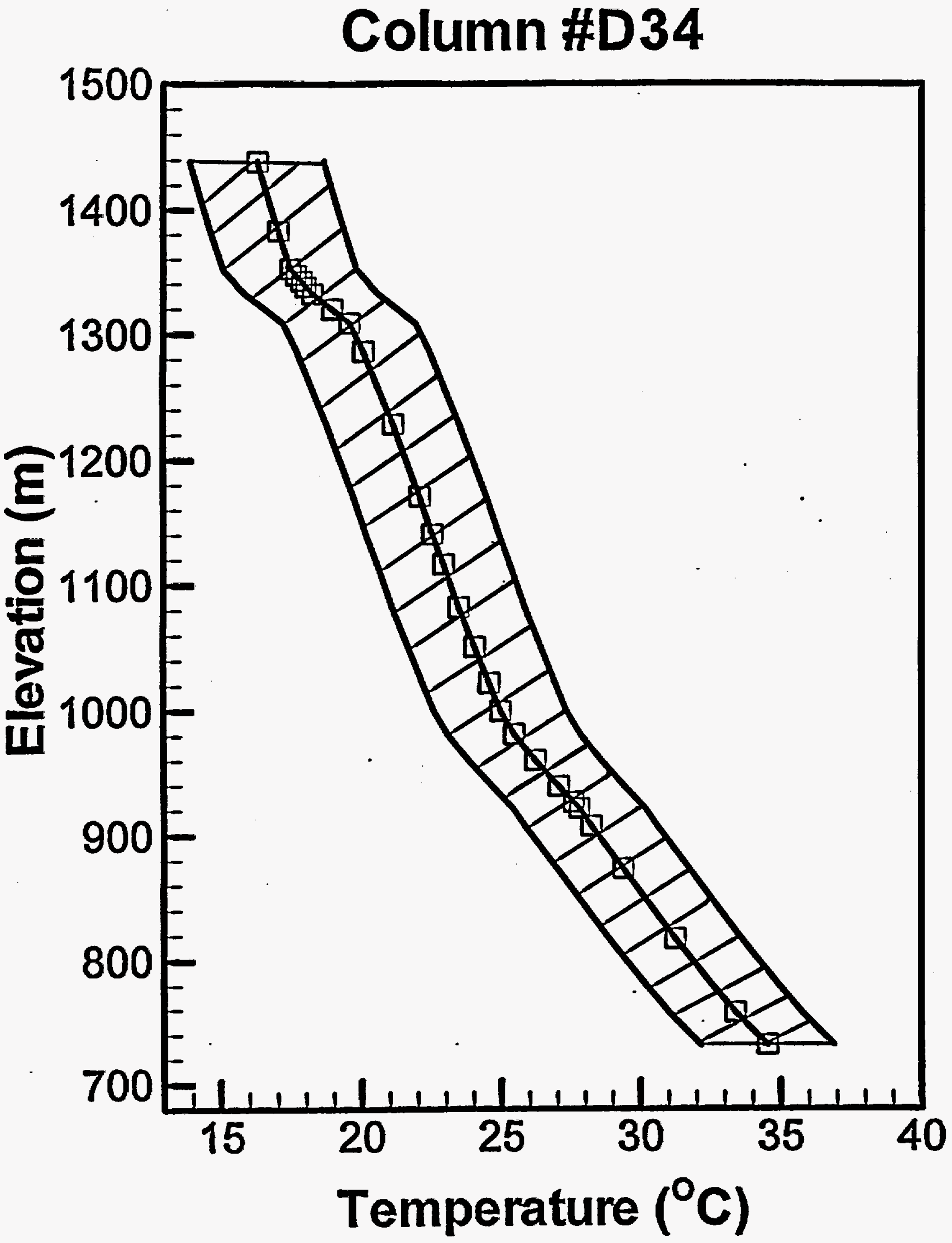

· **Figure 4.3-5 Simulated 1-D temperature profile along Column D34 extracted from the 3-D model.**

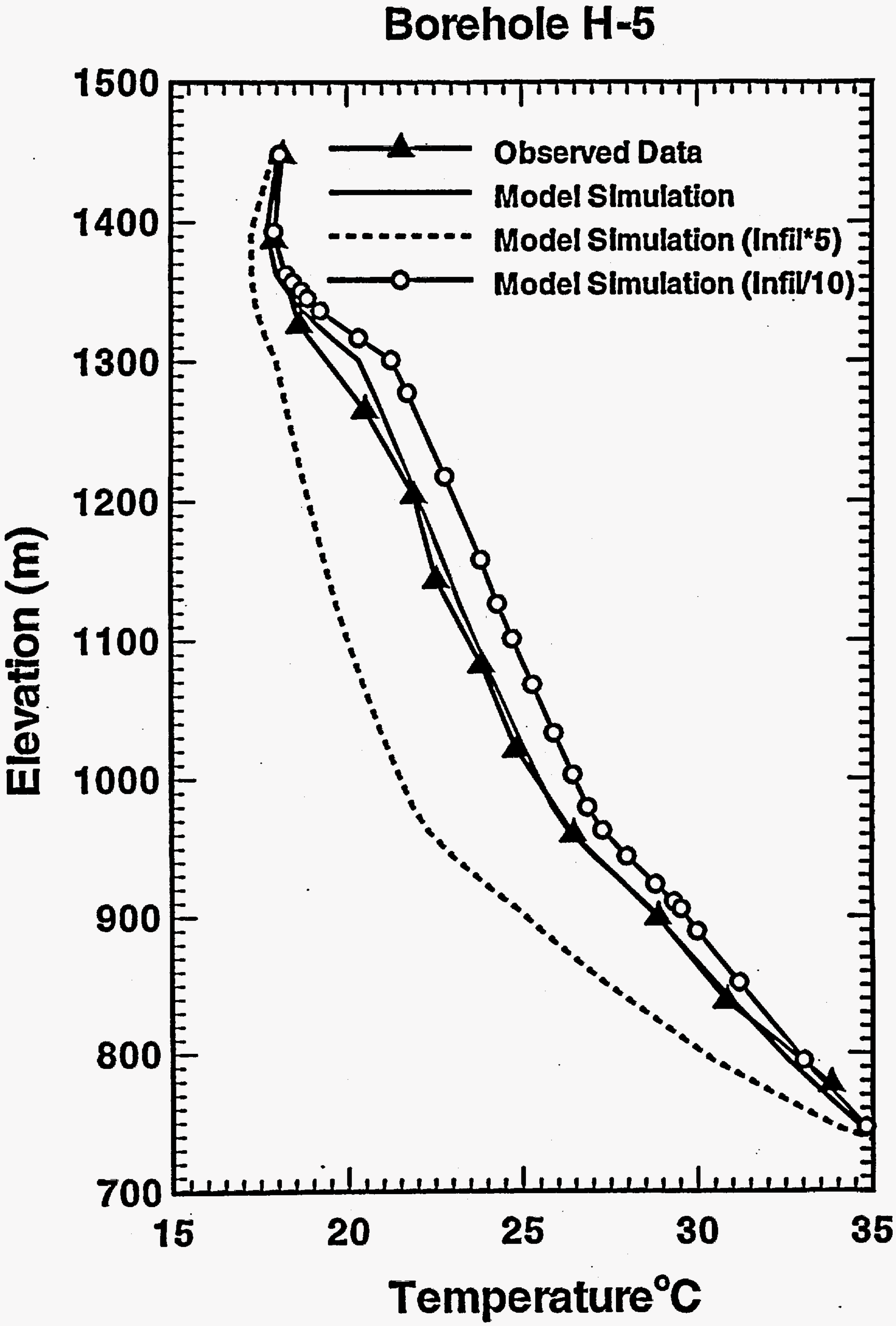

Figure 4.3-6: 1-D temperature profile at borehole H-5 showing the range in temperatures predicted for the base-case, infiltration increased five-fold and infiltration decreased ten-fold scenarios.

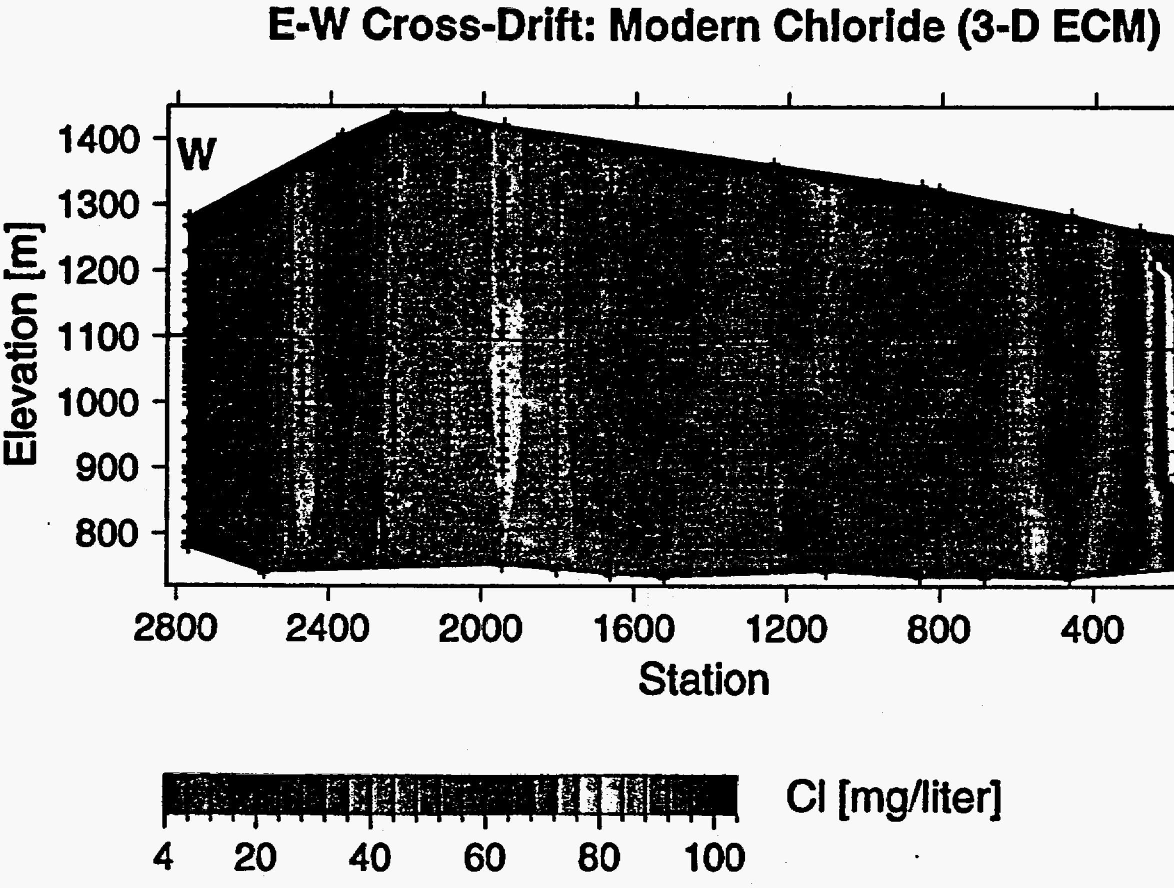

Figure 4.4-1. Cross section along the cross-drift through the 3-D ECM submodel grid. Chloride concentrations are steady-state distributions for the modern precipitation and infiltration rates.

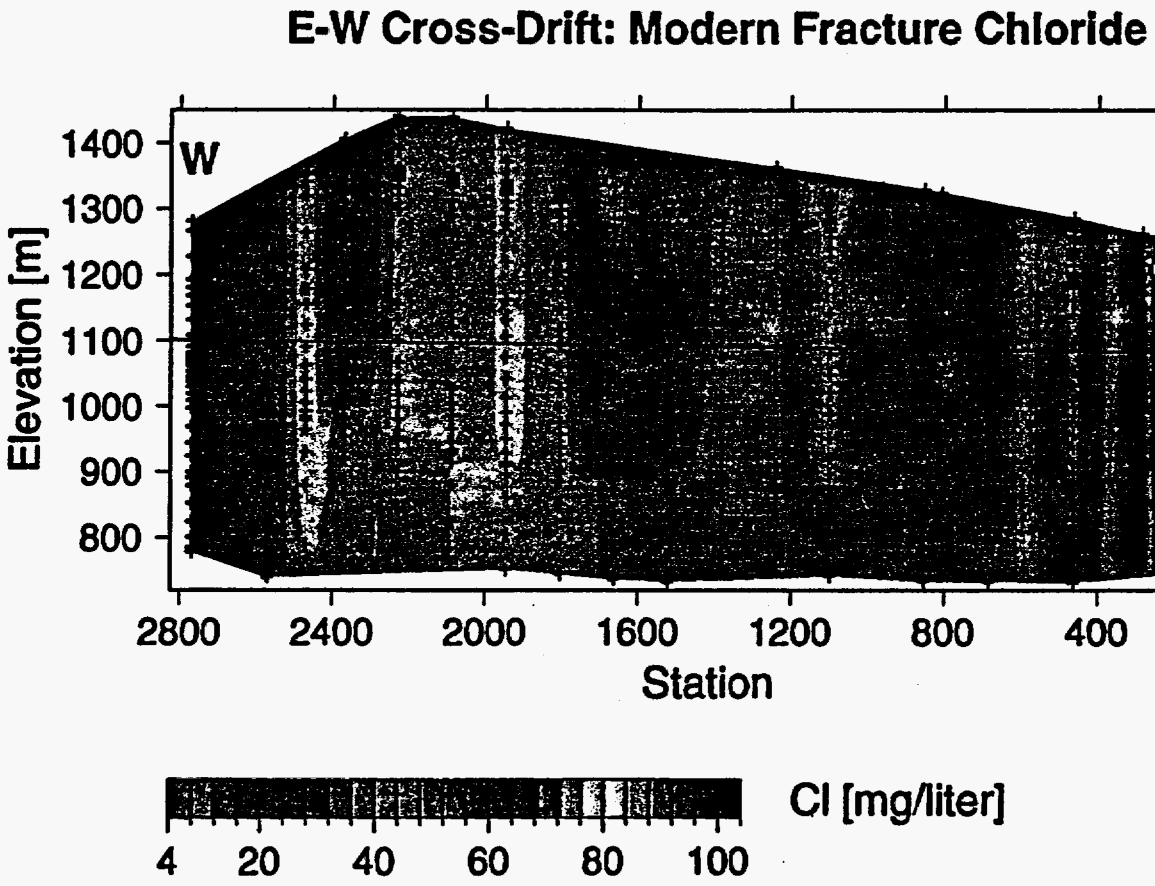

Figure 4.4-2. 2-D cross section along the cross-drift using the dual-permeability grid. Chloride concentrations in fractures are steady-state distributions for the modern precipitation and infiltration rates. Matrix concentrations are nearly the same for these steady-state conditions.

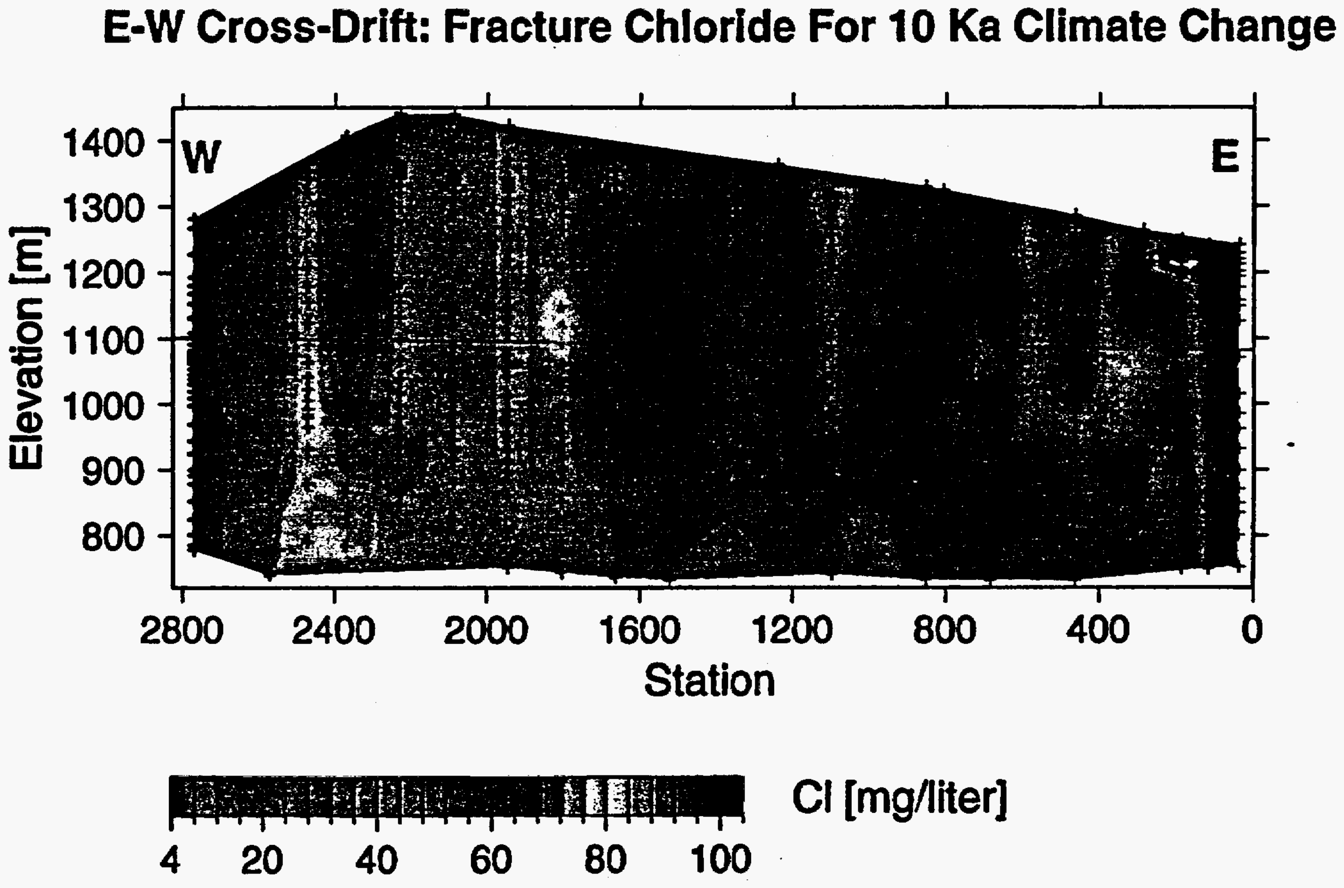

Figure 4.4-3. 2-D cross section along the cross-drift using the dual-permeability grid. Chloride concentrations in fractures are shown for transient case of modern precipitation and infiltration rates applied to the steady-state glacial maximum distributions.

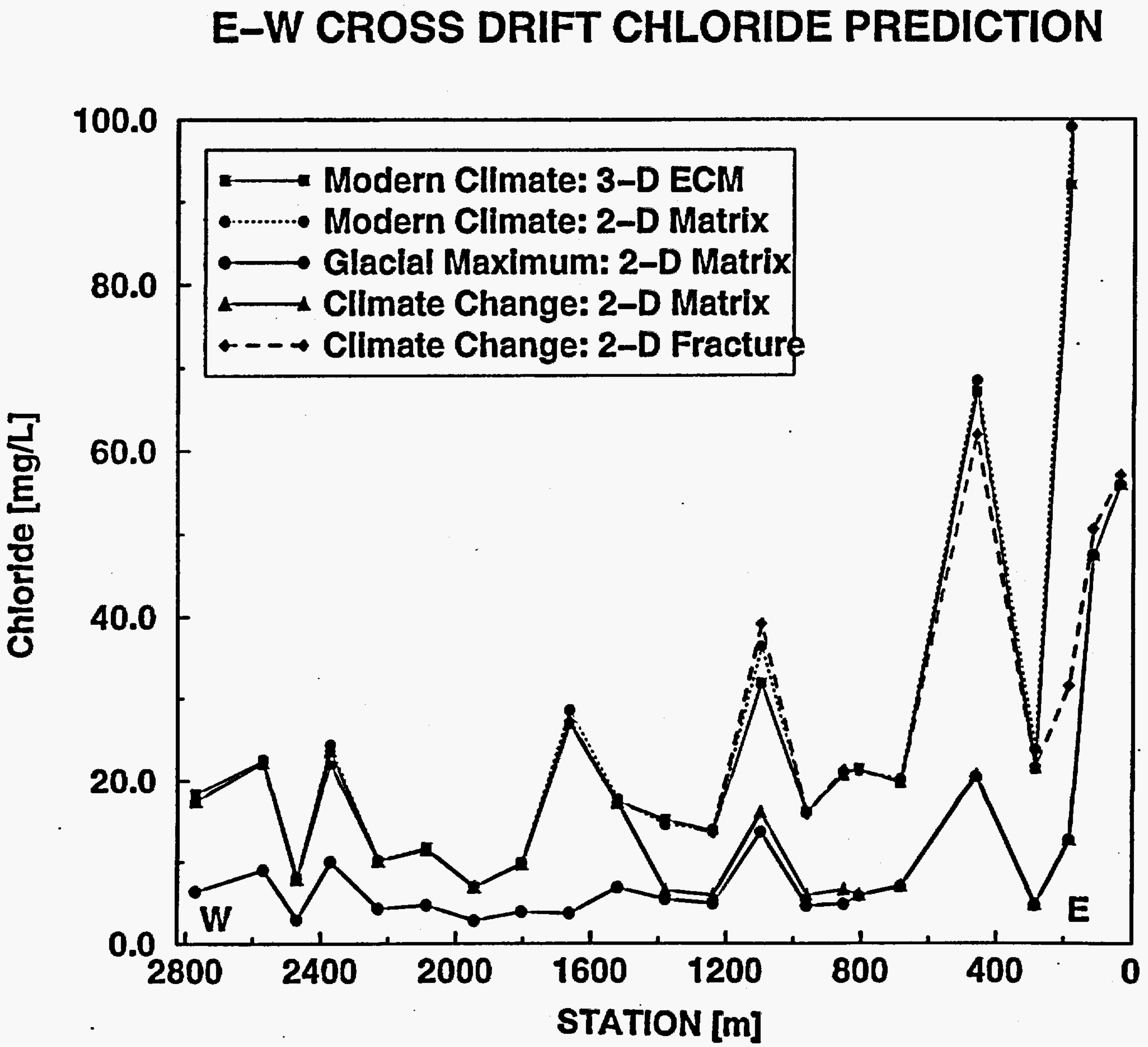

Figure 4.4-4. Chloride concentrations plotted along the cross-drift. Values at the margin plot off the y-axis and are not considered reliable.

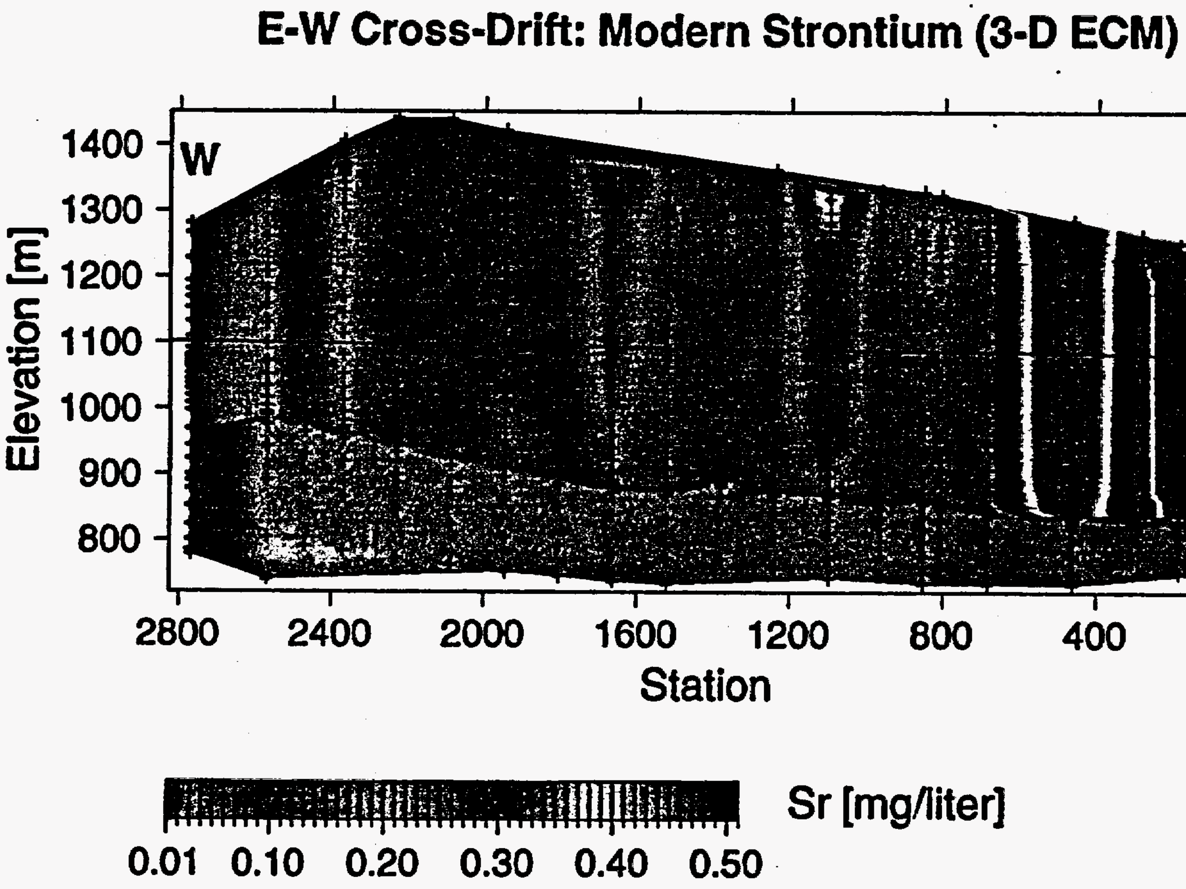

Figure 4.4-5. Cross section along the cross-drift through the 3-D ECM submodel grid. Strontium concentrations are steady-state distributions for the modern precipitation and infiltration rates.

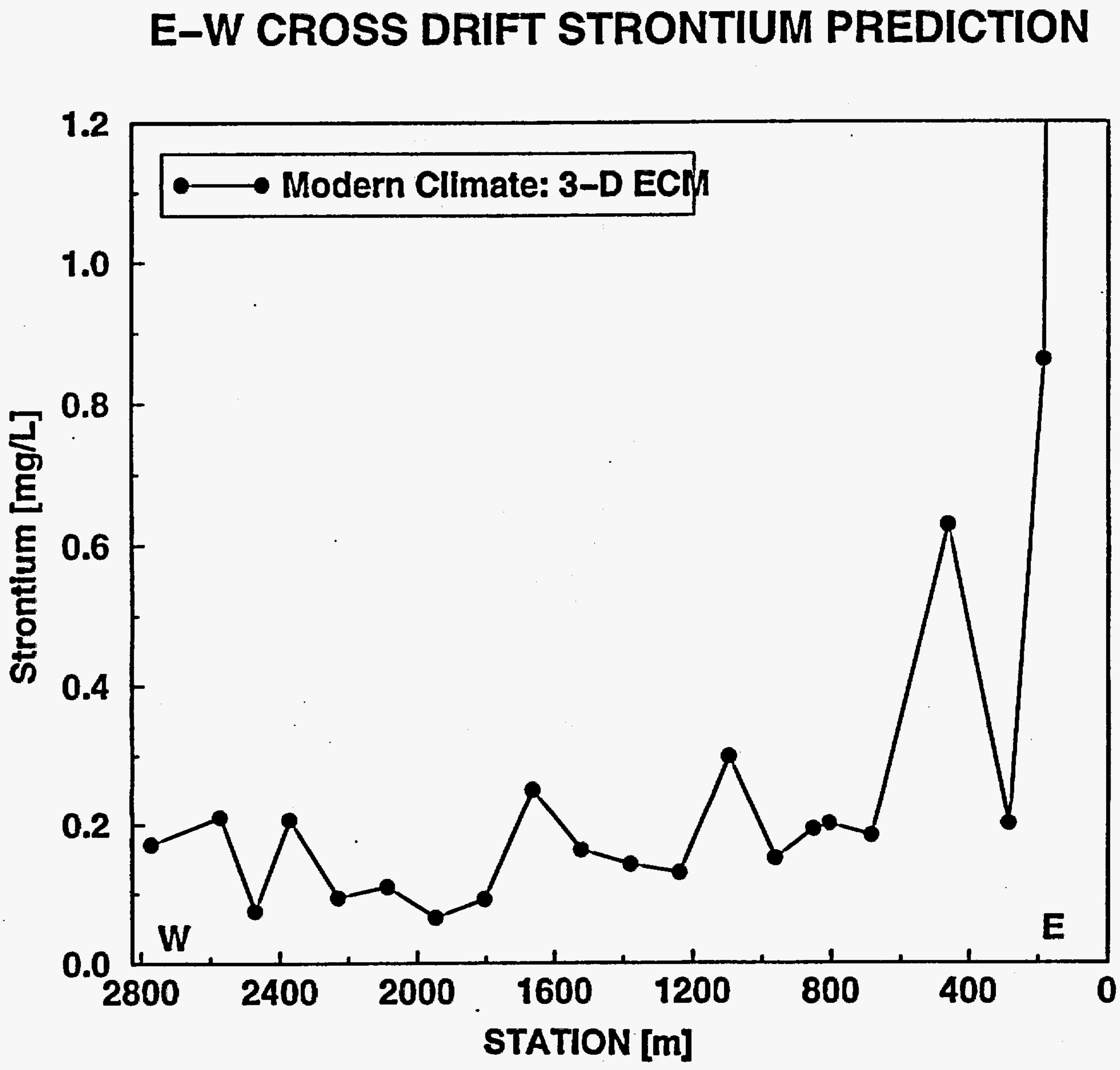

Figure 4.4-6. Strontium concentrations plotted along the cross-drift.

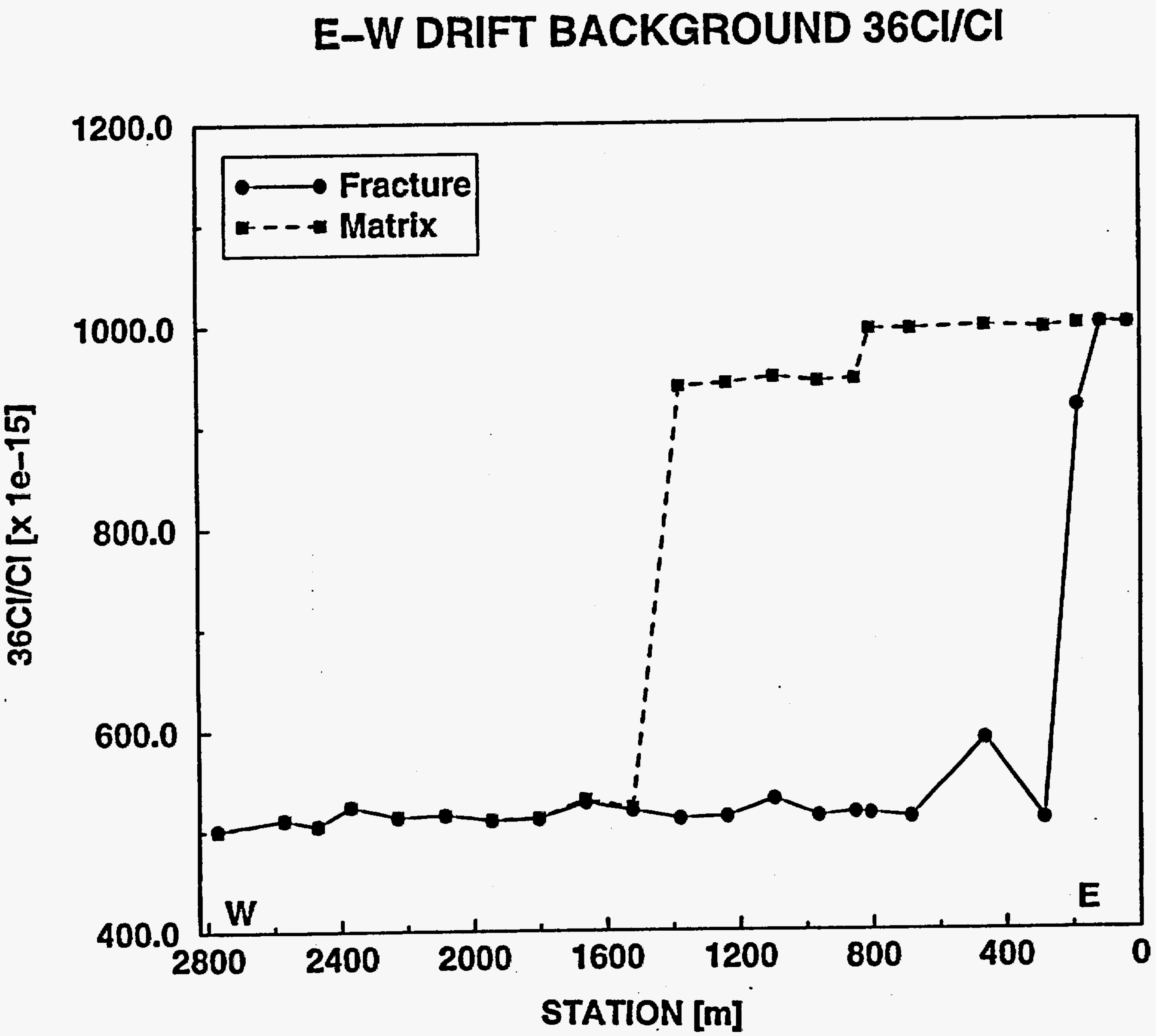

Figure 4.4-7. Estimated background ^{36}Cl/Cl concentrations plotted along the cross-drift.

Appendix A: Rock Properties

This appendix lists the rock property set used for the modeling conducted in this report. These parameter sets were previously presented in Bodvarsson et al., eds., 1997 and Wu et al., 1997. The rock properties for the fault and perched water zones are also included.

1. Tables A-1a and A-1b list the matrix and fracture rock properties, respectively, for the base-case, present day infiltration scenario (Qb) used for all simulations. Note that as discussed in Section 3.3, Model Parameters, the perched water properties were removed from the ECM sub-model and the dual-k 2-D cross section model parameter sets to increase computational efficiency. These properties were replaced with the normal, non-perched water properties.

2. Tables A-2a and A-2b list the matrix and fracture rock properties, respectively, for the faults used for all simulations.

3. Table A-3 lists the thermal properties used for the non-isothermal simulations (from Ho and Francis, 1997).

The following tables include additional layers and model blocks that are used to calibrated the 3-D model. The correspondence between layers and model blocks that are used in the 3-D and 1-D models is summarized below.

Table A-4. Rock names for perched water zone property specification.

3-D model layers	1-D inversion layers	3-D model layers	1-D inversion layers
X= M for matrix, F for fractures			
ch3vc	ch2vc	pcX37	tsw37
ch4vc	ch2vc	pcX1z	ch1zc
ch4zc	ch3zc	pcX2z	ch2zc
bf3vb	pp3vp	pcX62	ch2zc
tm3vt	pp3vp	pcX3z	ch3zc
bf2zb	pp2zp	pcX4z	ch4zc
		chaXd	ch2vc

The major faults in the UZ model (Ghost Dance, Dune Wash, Iron Ridge and Solitario Canyon) are incorporated by assigning a group of matrix and fracture parameters to each hydrogeologic unit (TCw, PTn, TSw, and CHn) that is intersected by the fault. The following table summarizes the relationship between the fault model properties and the hydrogeologic units.

Table A-5. Rock names for fault zone specification.

3-D Fault Model Block	Hydrogeologic Unit	3-D Fault Model Block	Hydrogeologic Unit
X= M for matrix, F for fractures			
Ghost Dance Fault		Dune Wash Fault	
tcwXg	TCw	tcwXd	TCw
ptnXg	PTn	ptnXd	PTn
tswXg	TSw	tswXd	TSw
chnXg	CHn	chnXd	CHn
Iron Ridge Fault		Solitario Canyon Fault	
tcwXi	TCw	tcwXs	TCw
ptnXi	PTn	ptnXs	PTn
tswXi	TSw	tswXs	TSw
chnXi	CHn	chnXs	CHn

Table A-1a. Qb: Base Case Matrix Properties

Model Layer / Block Name	matrix permeability (k_m) (m^2)	matrix porosity ϕ_m (-)	matrix van Genuchten alpha (α_m) (1/Pa)	matrix van Genuchten m (λ) m_m (-)	matrix residual saturation S_{lrm} (-)	matrix satiated saturation S_{lsm} (-)
tcw11	5.37E-18	0.066	1.18E-06	0.232	0.13	1.00
tcw12	5.37E-18	0.066	1.32E-06	0.236	0.13	1.00
tcw13	4.90E-17	0.140	6.46E-07	0.427	0.33	1.00
ptn21	3.09E-14	0.369	3.80E-05	0.231	0.10	1.00
ptn22	3.02E-15	0.234	8.71E-06	0.488	0.14	1.00
ptn23	8.32E-14	0.353	4.57E-05	0.287	0.17	1.00
ptn24	1.15E-13	0.469	4.27E-05	0.349	0.10	1.00
ptn25	2.46E-13	0.464	1.95E-04	0.279	0.10	1.00
tsw31	4.90E-17	0.042	1.00E-05	0.237	0.11	1.00
tsw32	2.75E-16	0.146	2.29E-05	0.273	0.04	1.00
tsw33	1.15E-17	0.135	6.76E-06	0.248	0.06	1.00
tsw34	4.07E-18	0.089	1.02E-06	0.322	0.18	1.00
tsw35	1.55E-17	0.115	3.31E-06	0.229	0.08	1.00
tsw36	8.91E-17	0.092	7.41E-07	0.414	0.18	1.00
tsw37	1.29E-17	0.020	1.55E-06	0.387	0.50	1.00
ch1zc	1.38E-17	0.193	8.32E-07	0.366	0.36	1.00
ch2zc	9.12E-18	0.240	1.95E-06	0.220	0.20	1.00
ch3zc	9.12E-18	0.240	1.95E-06	0.220	0.20	1.00
ch4zc	1.55E-17	0.169	7.76E-07	0.477	0.33	1.00
ch1vc	1.32E-12	0.265	6.61E-05	0.190	0.04	1.00
ch2vc	2.57E-13	0.321	7.41E-05	0.224	0.06	1.00
ch3vc	2.57E-13	0.321	7.41E-05	0.224	0.06	1.00
ch4vc	2.57E-13	0.321	7.41E-05	0.224	0.06	1.00
pp3vp	2.82E-15	0.274	1.74E-05	0.311	0.07	1.00
bf3vb	2.82E-15	0.274	1.74E-05	0.311	0.07	1.00
tm3vt	2.82E-15	0.274	1.74E-05	0.311	0.07	1.00
pp2zp	5.75E-17	0.197	1.66E-06	0.316	0.18	1.00
bf2zb	5.75E-17	0.197	1.66E-06	0.316	0.18	1.00
tsw37/pcM37	6.08E-18	0.036	3.37E-07	0.372	0.20	1.00
ch1zc/pcM1z	5.40E-18	0.288	1.90E-07	0.359	0.36	1.00
ch2zc/pcM2z	4.50E-19	0.332	4.21E-06	0.228	0.20	1.00
ch2zc/pcM6z	4.50E-18	0.332	4.21E-06	0.228	0.20	1.00
ch3zc/pcM3z	4.50E-18	0.332	4.21E-06	0.228	0.20	1.00
ch4zc/pcM4z	8.40E-18	0.266	1.50E-07	0.476	0.33	1.00

Table A-1b. Qb: Base Case Fracture Properties

Model Layer/ Block Name	vertical fracture permeability (k) (m^2)	horizontal fracture permeability (k) (m^2)	fracture porosity φ (-)	fracture van Genuchten alpha (α) (1/Pa)	fracture van Genuchten m (λ) m (-)	fracture residual saturation S_{lrf} (-)	fracture satiated saturation S_{lsf} (-)	fracture frequency f (1/m)	fracture-matrix connection area modification factor (Λ) (-)
tcw11	2.29E-11	6.21E-12	2.33E-04	2.95E-04	0.492	0.01	1.00	1.020	4.9E-04
tcw12	1.38E-11	6.03E-12	2.99E-04	2.95E-04	0.492	0.01	1.00	1.830	4.9E-04
tcw13	2.82E-12	2.40E-13	7.05E-05	9.12E-05	0.492	0.01	1.00	1.270	4.9E-04
ptn21	5.25E-13	5.25E-13	4.84E-05	1.10E-03	0.492	0.01	1.00	0.870	1.1E-01
ptn22	1.95E-13	1.95E-13	4.83E-05	1.82E-03	0.492	0.01	1.00	0.290	7.1E-01
ptn23	2.57E-13	2.57E-13	1.30E-04	3.39E-03	0.492	0.01	1.00	0.290	6.9E-01
ptn24	6.17E-14	6.17E-14	6.94E-05	9.33E-04	0.492	0.01	1.00	0.630	4.8E-01
ptn25	7.76E-14	7.76E-14	3.86E-05	1.95E-04	0.279	0.01	1.00	0.650	4.8E-01
tsw31	1.07E-11	1.00E-12	8.92E-05	3.98E-05	0.481	0.01	1.00	1.100	5.0E-01
tsw32	1.51E-11	7.08E-13	1.29E-04	9.33E-05	0.488	0.01	1.00	1.010	2.9E-05
tsw33	2.63E-11	8.91E-13	1.05E-04	1.78E-04	0.492	0.01	1.00	0.690	7.9E-05
tsw34	6.76E-12	4.27E-13	1.24E-04	9.77E-05	0.492	0.01	1.00	1.880	1.5E-04
tsw35	3.80E-12	9.12E-13	3.29E-04	1.10E-04	0.492	0.01	1.00	1.810	7.8E-02
tsw36	1.20E-12	1.20E-12	3.99E-04	1.32E-04	0.492	0.01	1.00	2.100	4.8E-05
tsw37	1.20E-12	1.20E-12	4.92E-04	1.18E-04	0.492	0.01	1.00	2.880	4.9E-04
ch1zc	2.40E-14	2.40E-14	1.10E-05	1.12E-03	0.492	0.01	1.00	0.067	1.8E-01
ch2zc	1.18E-14	1.18E-14	1.10E-05	1.23E-03	0.492	0.01	1.00	0.067	1.0E+00
ch3zc	1.18E-14	1.18E-14	1.10E-05	1.23E-03	0.492	0.01	1.00	0.067	1.0E+00
ch4zc	1.55E-14	1.55E-14	1.10E-05	1.15E-03	0.492	0.01	1.00	0.067	5.0E-01
ch1vc	1.74E-13	1.74E-13	7.14E-05	1.18E-03	0.492	0.01	1.00	0.420	4.9E-01
ch2vc	2.88E-13	2.88E-13	7.14E-05	1.18E-03	0.492	0.01	1.00	0.420	4.9E-01
ch3vc	2.88E-13	2.88E-13	7.14E-05	1.18E-03	0.492	0.01	1.00	0.420	4.9E-01
ch4vc	2.88E-13	2.88E-13	7.14E-05	1.18E-03	0.492	0.01	1.00	0.420	4.9E-01
pp3vp	6.92E-13	6.92E-13	7.14E-05	1.41E-03	0.492	0.01	1.00	0.420	5.1E-04
bf3vb	6.92E-13	6.92E-13	7.14E-05	1.41E-03	0.492	0.01	1.00	0.420	5.1E-04
tm3vt	6.92E-13	6.92E-13	7.14E-05	1.41E-03	0.492	0.01	1.00	0.420	5.1E-04
pp2zp	6.46E-14	6.46E-14	1.10E-05	3.72E-04	0.492	0.01	1.00	0.067	4.9E-01
bf2zb	6.46E-14	6.46E-14	1.10E-05	3.72E-04	0.492	0.01	1.00	0.067	4.9E-01
tsw37/pcF37	3.04E-18	3.04E-18	1.10E-05	3.37E-07	0.372	0.20	1.00	0.067	1.0E+00
ch1zc/pcF1z	1.20E-17	1.20E-17	1.10E-05	1.90E-07	0.359	0.36	1.00	0.067	1.0E+00
ch2zc/pcF2z	3.50E-18	3.50E-18	1.10E-05	4.21E-06	0.228	0.20	1.00	0.067	1.0E+00
ch2zc/pcF62	4.50E-18	4.50E-18	1.10E-05	4.21E-06	0.228	0.20	1.00	0.067	1.0E+00
ch3zc/pcF3z	4.50E-18	4.50E-18	1.10E-05	4.21E-06	0.228	0.20	1.00	0.067	1.0E+00
ch4zc/pcF4z	8.40E-18	8.40E-18	1.10E-05	1.50E-07	0.476	0.33	1.00	0.067	1.0E+00

Table A-2a. Qb: Fault Matrix Properties

Model Block	matrix permeability (k_m) (m^2)	matrix porosity ϕ_m (-)	matrix van Genuchten alpha (α_m) (1/Pa)	matrix van Genuchten m (λ) m_m (-)	matrix residual saturation S_{lrm} (-)	matrix satiated saturation S_{lsm} (-)
tcwMg	1.00E-13	0.200	6.10E-05	0.500	0.00	1.00
ptnMg	1.00E-13	0.200	6.10E-05	0.500	0.00	1.00
tswMg	1.00E-13	0.200	6.10E-05	0.500	0.00	1.00
chnMg	5.00E-15	0.200	6.10E-05	0.500	0.00	1.00
tcwMl	1.00E-13	0.200	6.10E-05	0.500	0.00	1.00
ptnMl	1.00E-13	0.200	6.10E-05	0.500	0.00	1.00
tswMl	1.00E-13	0.200	6.10E-05	0.500	0.00	1.00
chnMl	5.00E-15	0.200	6.10E-05	0.500	0.00	1.00
tcwMd	1.00E-13	0.200	6.10E-05	0.500	0.00	1.00
ptnMd	1.00E-13	0.200	6.10E-05	0.500	0.00	1.00
tswMd	1.00E-13	0.200	6.10E-05	0.500	0.00	1.00
chnMd	5.00E-15	0.200	6.10E-05	0.500	0.00	1.00
chaMd	2.55E-13	0.100	1.39E-06	0.225	0.06	1.00
tcwMs	1.00E-13	0.050	2.00E-05	0.500	0.00	1.00
ptnMs	1.00E-13	0.050	2.00E-05	0.500	0.00	1.00
tswMs	1.00E-13	0.050	2.00E-05	0.500	0.00	1.00
chnMs	5.00E-14	0.100	2.00E-05	0.500	0.00	1.00